Correlations to predict turbulent streamwise influence regions and onset of transition in supersonic flows

by

Manohari D. Ramesh

A dissertation submitted to the graduate faculty

in partial fulfillment of the requirements for the degree of

DOCTOR OF PHILOSOPHY

Major: Aerospace Engineering

Program of Study Committee:
John C. Tannehill, Major Professor
Alric Rothmayer
Richard Pletcher
Ganesh Rajagopalan
Ambar Mitra

Iowa State University

Ames, Iowa

2003

Graduate College
Iowa State University

This is to certify that the Doctoral dissertation of

Manohari D. Ramesh

has met the dissertation requirements of Iowa State University

Signature was redacted for privacy.

Committee Member

Signature was redacted for privacy.

Committee Member

Signature was redacted for privacy.

Committee Member

Signature was redacted for privacy.

Committee Member

Signature was redacted for privacy.

Major Professor

Signature was redacted for privacy.

For the Major Program

TABLE OF CONTENTS

LIST OF FIGURES

LIST OF TABLES

ACKNOWLEDGMENTS

I would like to express my appreciation and thanks to my major professor, Dr. John C. Tannehill for his encouragement and guidance throughout my graduate study and research. My thanks also go out to Iowa State University and the Department of Aerospace Engineering for providing financial support during my graduate studies.

I would also like to thank my family, "Tubbs" for our Scrabble games and my trips to Swargam, "Big Bull" for providing constant entertainment and "Chipi 1" for her support of Tanthony pigs.

ABSTRACT

Correlation functions have been developed to predict both the extent of the streamwise influence regions in supersonic turbulent flows, and the onset of transition in supersonic flow past a flat plate. These correlations are empirical relations involving *a priori* known flow parameters. In the turbulent flow regime, correlations that can compute the extent of the upstream and downstream regions of influence in two-dimensional compression ramp and expansion corner flowfields have been developed. The correlations were obtained by analyzing numerically computed flowfields. Regression analysis using the least squares approach was applied to the computed flowfield data to determine the correlation functions. The turbulent correlations can be used in conjunction with an iterative parabolized Navier-Stokes algorithm to minimize the region of iteration and thereby reduce the computational time. In the transitional region, correlation functions that can accurately predict the onset of transition over a flat plate have been determined in a similar manner. The transitional correlations can be used in conjunction with any flow solver in order to automatically determine the onset of transition and apply a turbulence model for closure at the appropriate location. The general form of these correlation functions, the wide range of applicability, and their ease of calculation makes them a handy tool for engineering design purposes. The accuracy of these functions is demonstrated by comparing them with experimental and empirical data available in the literature.

1 INTRODUCTION

Overview

Many practical flowfields in the supersonic regime involve design problems which are caused by the presence of shock and expansion waves in the flowfield. The problems caused by the presence of shock and expansion waves in two-dimensional (2-D) supersonic flows are compounded in turbulent flows, as turbulence adds to the complexity of the flow. Shock waves and expansion waves in a flowfield result from a change in geometry (such as a compression ramp or an expansion corner) or from an externally generated shock impinging on the aircraft's body. The viscous-inviscid interaction in the boundary layer in the presence of a shock distorts the structure of the boundary layer, leading to the generation of compression and expansion waves which travel through out the flow field. The elliptic nature of the boundary layer below the sonic line results in an upstream influence, which alters the flow through the shock and results in a complex interaction mechanism, wherein a slight disturbance in any of the flow conditions results in considerable alteration of the flow structure in the boundary layer. Thus, design of a supersonic vehicle under such adverse conditions would be greatly facilitated if information about the extent of the streamwise interaction is known *a priori*.

Transition of supersonic flow from a laminar to a turbulent regime has a marked effect on the airflow over aerodynamic bodies. Lack of proper prediction of the onset of transition can lead to the inaccurate prediction of skin friction and hence to erroneous results for the drag and local heating of aerodynamic surfaces. These problems are compounded by the dearth of easily applicable design tools, which could be used to provide an engineering estimate of the flow properties in supersonic transitional flow regions. Prediction of transition is also important from a purely numerical standpoint. Many of the current computational codes

utilize turbulence models to model the turbulent flow. This requires the prior specification of regions of laminar and turbulent flow in order to apply the turbulence models appropriately, as most of the turbulence models do not have a mechanism to automatically determine the nature of the flow. Therefore, the design of a supersonic vehicle would be greatly facilitated if information about the onset of transition is known *a priori.*

Correlation functions

Turbulent streamwise influence regions

Several attempts have been made to correlate the upstream influence region in a 2-D turbulent flow over a compression ramp, for example Refs. [1, 2, 3, 4]. Numerous experiments have also been conducted for a wide variety of compression ramp flowfields, for example Refs. [1]-[12]. Settles et al. [2, 3] have performed the most notable work in correlating the upstream influence region in the presence of a compression ramp, based on the "upstream pressure influence" criterion. These investigators dealt with the relationship between the upstream influence length and the Reynolds number and/or the angle of the compression ramp, but did not address the effects of the variation of Mach number. The correlation developed by Roshko and Thomke [4] requires the determination of the skin-friction coefficient prior to computing the downstream influence length. These limitations rule out the use of these relations for the *a priori* determination of the streamwise influence lengths.

Some work has been performed to develop correlations for the streamwise influence regions of an expansion corner flow. Chung [13] and Lu and Chung [14] have considered the flow over an expansion corner and have developed a downstream influence scaling for the turbulent flow past expansion corners. However, the scaling does not address the variation of Reynolds number, and hence is limited in its application. Chew [15] has presented experimental results for the shock-wave boundary-layer interaction in the presence of an expansion corner. Narasimha and Sreenivasan [16] have presented results on the relaminarization of expansion corner flows.

The absence of adequate and accurate theoretical, empirical or experimental relations, relating the streamwise influence lengths with the known flow parameters for a 2-D supersonic

turbulent flow over a compression ramp and expansion corner, was the impetus for the current study. Correlations functions for the case of an externally generated shock impinging on a flat plate have been developed previously by the present author [17, 18].

Onset of transition

A literature survey of the research on predicting the onset of transition yields experimental, theoretical and empirical results, for example Refs.[19]-[32]. These investigations have dealt with the effects of Mach number, Reynolds number, surface roughness, suction, pressure gradient, etc, for various geometries. Extensive data based on stability analysis is also currently available. However, the mathematical complexity of this approach increases tremendously when several flow parameters are considered simultaneously. Also, the predictions from the stability analysis do not relate well with experimental observations. Another approach applicable to transition of supersonic flow over a flat plate is the use of e^N methods. In addition to these approaches, several methods have been developed to model the transitional flow region using one-equation models [33], intermittency functions [34, 35], transition corrections to turbulent models [36], DNS simulations [37, 38], etc.

A significant amount of work has been performed on correlating cone and flat plate transition Reynolds numbers in supersonic and hypersonic flows. Pate [24, 25] investigated the influence of aerodynamic noise effects in various wind tunnels on boundary-layer transition. Results for two-dimensional planar bodies and slender cones were presented, and equations relating transition Reynolds number with the skin-friction coefficient, boundary-layer displacement thickness, and wind tunnel parameters were developed. However, since the skin-friction coefficient at transition is normally unknown, this rules out the use of the developed correlation as a practical tool. Chen [22, 23] has compared the transition on a cone and flat plate at a Mach number of 3.5. Abu-Ghannam [39] has developed a correlation to predict transition past a flat plate in subsonic flow.

Currently there is no general mathematical model which can provide an engineering estimate of natural transition in supersonic flow past a flat plate using only the basic *a priori*

known transition flow parameters [19, 20]. One obvious difficulty is the incomplete understanding of the variety of influences that can trigger transition. While acknowledging that a complex flow phenomenon like transition does not lend itself to a quick and easy method of prediction, some progress can be made at correlating the flow parameters which trigger transition in a practical way such that a good first estimate can be obtained. The aim of the current research is to provide an engineering estimate of the onset of transition for a supersonic flat-plate flow.

Determination of correlation functions

The current study generates the supersonic flowfield data numerically, and then validates the numerical data with experimental and empirical data available in the literature. The numerically generated data are then used to develop empirically determined correlation functions that predict the onset of transition and the extent of streamwise turbulent regions of influence, based on an *a priori* knowledge of parameters such as Mach number (M_∞), Reynolds number (Re_∞), pressure gradient across the flowfield ($\Delta p/p_\infty$) and the freestream turbulence intensity (Ti_∞). Regression analysis is applied to the numerically generated data to determine the correlation functions.

The supersonic flowfields were computed using the TIPNS algorithm developed by Tannehill et al. [40]. The transitional flow is modeled using the two-equation $k-\omega$ turbulence model of Wilcox [36]. The turbulent flow is modeled using the relaxation eddy viscosity model of Shang and Hankey [41, 42], which consists of a simple modification to an algebraic model.

Since the correlations developed in this study are based only on previously known flow parameters, they will facilitate the determination of the onset of transition and the extent of the turbulent streamwise regions of influence without any numerical computations. In addition, the newly developed correlations could be coupled with those developed previously for both laminar [43] and turbulent flow [17, 18] in order to automate the computation of various flowfields.

2 GOVERNING EQUATIONS

The equations governing the flow field are the complete Navier Stokes (NS) equations. However, these equations are cumbersome to deal with, both in terms of memory requirements and time to obtain a solution. A subset of the NS equations are the parabolized Navier Stokes (PNS) equations, which are derived from the NS equations by dropping the unsteady terms and the streamwise viscous terms. The governing equations for the present study are the compressible PNS equations. The transitional flow is governed by the $k-\omega$ turbulence model of Wilcox [36] and turbulence closure is provided by the relaxation eddy viscosity model [41, 42]. The governing equations for the turbulence model and the transitional model are presented in Chapter 4. The PNS equations, in a 3D coordinate system (ξ, η, ζ) are

$$\mathbf{E}_\xi + \mathbf{F}_\eta + \mathbf{G}_\zeta = 0 \tag{2.1}$$

where

$$\begin{aligned}
\mathbf{E} &= \frac{1}{J}\left[\ \xi_x\mathbf{E_i} + \xi_y\mathbf{F_i} + \xi_z\mathbf{G_i}\ \right] \\
\mathbf{F} &= \frac{1}{J}\left[\ \eta_x(\mathbf{E_i}-\mathbf{E'_v}) + \eta_y(\mathbf{F_i}-\mathbf{F'_v}) + \eta_y(\mathbf{G_i}-\mathbf{G'_v})\ \right] \\
\mathbf{G} &= \frac{1}{J}\left[\ \zeta_x(\mathbf{E_i}-\mathbf{E'_v}) + \zeta_y(\mathbf{F_i}-\mathbf{F'_v}) + \zeta_z(\mathbf{G_i}-\mathbf{G'_v})\ \right]
\end{aligned} \tag{2.2}$$

In the above equations, the subscript '**i**' refers to the inviscid terms, subscript '**v**' refers to the viscous terms and the primed ($'$) quantities represent the terms wherein the streamwise (ξ direction) viscous terms have been dropped, and J is the Jacobian of the transformation. The inviscid and viscous flux vectors are given by

$$\mathbf{E_i} = \left[\ \rho u, \rho u^2 + p, \rho uv, \rho uw, (E_t + p)u\ \right]^T$$

$$\mathbf{F_i} = \left[\rho v, \rho uv, \rho v^2 + p, \rho vw, (E_t + p)v \right]^T$$

$$\mathbf{G_i} = \left[\rho w, \rho uw, \rho vw, \rho w^2 + p, (E_t + p)w \right]^T$$

$$\mathbf{E_v} = \left[0, \tau_{xx}, \tau_{xy}, \tau_{xz}, u\tau_{xx} + v\tau_{xy} + w\tau_{xz} - q_x \right]^T$$

$$\mathbf{F_v} = \left[0, \tau_{xy}, \tau_{yy}, \tau_{yz}, u\tau_{xy} + v\tau_{yy} + w\tau_{yz} - q_y \right]^T$$

$$\mathbf{G_v} = \left[0, \tau_{xz}, \tau_{yz}, \tau_{zz}, u\tau_{xz} + v\tau_{yz} + w\tau_{zz} - q_z \right]^T$$

The total energy, E_t is given by

$$E_t = \rho \left[e + \tfrac{1}{2}(u^2 + v^2 + w^2) \right]$$

The system of equations is closed by the perfect gas law

$$p = (\gamma - 1)\rho e$$

and the laminar viscosity is calculated using Sutherland's law

$$\mu = C_1 \frac{T^{3/2}}{T + C_2}$$

where $C_1 = 1.458 \times 10^{-6} kg/(ms\sqrt{k})$ and $C_2 = 110.4$ K. A laminar Prandtl number of 0.7 and a turbulent Prandtl number of 0.9 is used in the computations.

In the streamwise direction, the PNS equations are hyperbolic-parabolic in character provided that (a) the flow is attached, (b) the inviscid flowfield is supersonic, and (c) the streamwise pressure gradient is either neglected in the subsonic region or altered to suppress the departure behavior. The Vigneron [44] technique has often been used to suppress departure solutions. The Vigneron parameter ω is given by

$$\omega = min\left[1, \frac{\sigma\gamma {M_\xi}^2}{1 + (\gamma - 1)M_\xi^2}\right]$$

where M_ξ is the local Mach number in the ξ direction and σ is a safety factor. Using the Vigneron parameter, the vector $\mathbf{E}$ may be written as

$$\mathbf{E} = \mathbf{E}^* + \mathbf{E}^p \tag{2.3}$$

where

$$\mathbf{E}^* = \frac{\xi_x}{J}\begin{bmatrix} \rho u \\ \rho u^2 + \omega p \\ \rho uv \\ \rho uw \\ (E_t + p)u \end{bmatrix} + \frac{\xi_y}{J}\begin{bmatrix} \rho v \\ \rho uv \\ \rho v^2 + \omega p \\ \rho vw \\ (E_t + p)v \end{bmatrix} + \frac{\xi_z}{J}\begin{bmatrix} \rho w \\ \rho uw \\ \rho vw \\ \rho w^2 + \omega p \\ (E_t + p)w \end{bmatrix}$$

and

$$\mathbf{E}^p = \frac{\xi_x}{J}\begin{bmatrix} 0 \\ (1-\omega)p \\ 0 \\ 0 \\ 0 \end{bmatrix} + \frac{\xi_y}{J}\begin{bmatrix} 0 \\ 0 \\ (1-\omega)p \\ 0 \\ 0 \end{bmatrix} + \frac{\xi_z}{J}\begin{bmatrix} 0 \\ 0 \\ 0 \\ (1-\omega)p \\ 0 \end{bmatrix}$$

To avoid departure solutions in the subsonic portion of the flowfield, the "elliptic" part of the streamwise pressure gradient ($\mathbf{E}^p$) is omitted. The PNS equations admit ellipticity in the crossflow planes, and hence any upstream effects occurring in the crossflow plane are automatically computed.

3 NUMERICAL ALGORITHM

UPS algorithm

The governing PNS equations were numerically solved using a finite-volume formulation with an upwind, TVD scheme based on Roe's approximate Riemann solver. This method for solving the PNS equations was developed by Lawrence et al. [45] and is used in NASA's UPS code. The PNS equations are well suited for the computation of attached, supersonic viscous flows. However since the PNS equations are solved using a single-sweep space-marching method, they are not suitable for the computation of flows with upstream influences. In order to compute flows with streamwise influence effects, modifications to the PNS algorithm must be made. This resulted in the development, by Miller et al. [46] and Tannehill et al. [40], of the IPNS and the TIPNS algorithms which can be used to compute flows with upstream/downstream influences.

PNS algorithm

The PNS algorithm is used in calculating attached flows with no noticeable upstream influence. The governing equation is given by Eq. (2.1) and the streamwise flux vector $\mathbf{E}$ is given by Eq. (2.3). The flux vectors at a given station ξ can be represented using the following notation

$$\mathbf{E}^{*}_{i+1} = \mathbf{E}^{*}(d\mathbf{S}_{i+1}, \mathbf{U}_{i+1})$$

$$\mathbf{E}^{p}_{i+1} = \mathbf{E}^{p}(d\mathbf{S}_{i+1}, \mathbf{U}_{i+1})$$

where the metrics (representing the geometry of the flowfield) are designated by $d\mathbf{S}_i$, and the subscript *(i+1)* represents the spatial index, in the ξ direction, at which the solution is being

computed. The first-order accurate expression for the streamwise flux vector $\mathbf{E}$ can then be written as

$$\left(\frac{\partial \mathbf{E}}{\partial \xi}\right)_{i+1} = \frac{1}{\Delta \xi}\left[(\mathbf{E^*}_{i+1} - \mathbf{E^*}_i) + (\mathbf{E^p}_{i+1} - \mathbf{E^p}_i)\right] \tag{3.1}$$

The $\mathbf{E^*}_{i+1}$ and $\mathbf{E^p}_{i+1}$ vectors are then linearized in the following manner

$$\mathbf{E}^*_{i+1} = \mathbf{E}^*(d\mathbf{S}_{i+1}, \mathbf{U}_i) + \frac{\partial \mathbf{E}^*(d\mathbf{S}_{i+1}, \mathbf{U}_i)}{\partial \mathbf{U}_i}(\mathbf{U}_{i+1} - \mathbf{U}_i)$$

$$\mathbf{E}^p_{i+1} = \mathbf{E}^p(d\mathbf{S}_{i+1}, \mathbf{U}_i) + \frac{\partial \mathbf{E}^p(d\mathbf{S}_{i+1}, \mathbf{U}_i)}{\partial \mathbf{U}_i}(\mathbf{U}_{i+1} - \mathbf{U}_i)$$

where the Jacobians can be represented by

$$A^*(d\mathbf{S}_{i+1}, \mathbf{U}_i) = \frac{\partial \mathbf{E}^*(d\mathbf{S}_{i+1}, \mathbf{U}_i)}{\partial \mathbf{U}_i}$$

$$A^p(d\mathbf{S}_{i+1}, \mathbf{U}_i) = \frac{\partial \mathbf{E}^p(d\mathbf{S}_{i+1}, \mathbf{U}_i)}{\partial \mathbf{U}_i}$$

Substituting the linearizations and the Jacobians into Eq. (3.1) and simplifying, the following expression for the streamwise gradient is obtained

$$\left(\frac{\partial \mathbf{E}}{\partial \xi}\right)_{i+1} = \frac{1}{\Delta \xi}\left\{\left[A^*(d\mathbf{S}_{i+1}, \mathbf{U}_i) + A^p(d\mathbf{S}_{i+1}, \mathbf{U}_i)\right]\left[\mathbf{U}_{i+1} - \mathbf{U}_i\right]\right.$$
$$\left. + \left[A(d\mathbf{S}_{i+1}, \mathbf{U}_i) - A(d\mathbf{S}_i, \mathbf{U}_i)\right]\mathbf{U}_i\right\}$$

where

$$A = A^* + A^p$$

For PNS calculations, the term $A^p(d\mathbf{S}_{i+1}, \mathbf{U}_i)$ is omitted to prevent departure solutions. Further details of this method can be found in Refs. [40, 43, 46].

Iterative PNS (IPNS) algorithm

Modifications to the PNS equations to enable capturing the upstream influence effects lead to the IPNS algorithm developed by Miller et al. [43, 46]. The IPNS algorithm has the capacity to accurately compute attached or separated supersonic viscous flows with upstream influence.

The IPNS method is obtained by using forward differencing for the elliptic portion of the streamwise gradient, thus capturing the upstream influence effects. The first-order accurate finite-volume expression for the streamwise gradient in the streamwise direction is

$$\left(\frac{\partial \mathbf{E}}{\partial \xi}\right)_{i+1} = \frac{1}{\Delta \xi}\left[\mathbf{E}^*{}_{i+1} - \mathbf{E}^*{}_i + \mathbf{E}^p(d\mathbf{S}_{i+1}, \mathbf{U}_{i+2}) - \mathbf{E}^p(d\mathbf{S}_i, \mathbf{U}_{i+1})\right] \tag{3.2}$$

where $\mathbf{U}_{i+2}$ is obtained from a previous sweep. Using appropriate linearizations and simplifications as used in the PNS scheme, the streamwise gradient is given by

$$\begin{aligned}\left(\frac{\partial \mathbf{E}}{\partial \xi}\right)_{i+1} = \frac{1}{\Delta \xi}\{&\left[A^*(d\mathbf{S}_{i+1}, \mathbf{U}_i) + A^p(d\mathbf{S}_{i+1}, \mathbf{U}_i)\right]\left[\mathbf{U}_{i+1} - \mathbf{U}_i\right] \\ &+ \left[A(d\mathbf{S}_{i+1}, \mathbf{U}_i) - A(d\mathbf{S}_i, \mathbf{U}_i)\right]\mathbf{U}_i \\ &+ A^p(d\mathbf{S}_{i+1}, \mathbf{U}_{i+1})\left[\mathbf{U}_{i+2} - \mathbf{U}_i\right]\}\end{aligned}$$

The last term of the above equation is replaced with the following approximation

$$A^p(d\mathbf{S}_{i+1}, \mathbf{U}_{i+1})\left[\mathbf{U}_{i+2} - \mathbf{U}_i\right] \approx \mathbf{E}^p(d\mathbf{S}_{i+1}, \mathbf{U}_{i+2}) - \mathbf{E}^p(d\mathbf{S}_{i+1}, \mathbf{U}_i)$$

For separated flow, the FLARE approximation is used and ω is set to zero in the boundary layer of the IPNS region. This results in the following definition for ω

$$\omega = \begin{cases} 0 & V \leq V_\delta \\ 1 & V > V_\delta \end{cases}$$

where V_δ is the velocity magnitude corresponding to the boundary-layer edge and is set to 0.99 of the freestream velocity. Details of the IPNS approach are given in Ref. [46].

Time Iterative PNS (TIPNS) algorithm

When the separated region becomes large, the IPNS approach is unable to accurately capture the extensive influence effects of the massively separated flow. Therefore, when the flow is severely separated, the TIPNS approach is used. The TIPNS approach developed by Tannehill et al. [40], uses the Steger-Warming flux splitting in the streamwise direction in place of the Vigneron splitting. The TIPNS method thus removes the necessity for the

FLARE approximation. The TIPNS equations are similar to the thin layer Navier-Stokes (TLNS) equations. However, the linearizations of the streamwise and crossflow fluxes in the TIPNS code are more appropriate to the space-marching technique, making it compatible with the space-marching approach of the IPNS technique. The unsteady term is discretized using a first-order difference, and the governing equation becomes

$$\frac{1}{J\Delta t}\left(\mathbf{U}^{n+1}-\mathbf{U}^{n}\right)+\mathbf{E}_{\xi}^{n+1}+\mathbf{F}_{\eta}^{n+1}+\mathbf{G}_{\zeta}^{n+1}=0 \tag{3.3}$$

where the superscript $(n+1)$ denotes the time level at which the solution is currently being computed and J is the Jacobian of the transformation. All the terms are computed at a spatial index of $(i+1)$. The above equation can be written as

$$\frac{1}{J\Delta t}\left(\mathbf{U}_{i+1}^{n+1}-\mathbf{U}_{i}^{n}\right)+\left(\frac{\partial\mathbf{E}}{\partial\xi}\right)_{i+1}^{n+1}+\left(\frac{\partial\mathbf{F}}{\partial\eta}\right)_{i+1}^{n+1}+\left(\frac{\partial\mathbf{G}}{\partial\zeta}\right)_{i+1}^{n+1}=-\frac{1}{J\Delta t}\left(\mathbf{U}_{i}^{n+1}-\mathbf{U}_{i+1}^{n}\right) \tag{3.4}$$

The $\mathbf{E}$ vector is split using the Steger-Warming flux splitting technique. i.e,

$$\mathbf{E}=\mathbf{E}^{+}+\mathbf{E}^{-}=A^{+}\mathbf{U}+A^{-}\mathbf{U} \tag{3.5}$$

where $\mathbf{E}^{+}$ and $\mathbf{E}^{-}$ are the positive and negative eigenvalues respectively and A^{+} and A^{-} are the Jacobians. The streamwise gradient of $\mathbf{E}$ is then discretized using a backward difference for $\mathbf{E}^{+}$ and a forward difference for $\mathbf{E}^{-}$. This same splitting can also be used in the IPNS approach. This results in the following expression for the streamwise flux vector $\mathbf{E}$

$$\begin{aligned}\left(\frac{\partial\mathbf{E}}{\partial\xi}\right)_{i+1}^{n+1} &= \left(\frac{\partial\mathbf{E}^{+}}{\partial\xi}\right)_{i+1}^{n+1}+\left(\frac{\partial\mathbf{E}^{-}}{\partial\xi}\right)_{i+1}^{n+1}\\ &= \frac{1}{\Delta\xi}\left\{\left[(\mathbf{E}^{+})_{i+1}^{n+1}-(\mathbf{E}^{+})_{i}^{n+1}\right]+\left[\mathbf{E}^{-}(d\mathbf{S}_{i+1},\mathbf{U}_{i+1}^{n})-\mathbf{E}^{-}(d\mathbf{S}_{i},\mathbf{U}_{i+1}^{n+1})\right]\right\}\end{aligned} \tag{3.6}$$

The final form of the algorithm is obtained by substituting the above equation into Eq. (3.4) and using linearizations and simplifications similar to the IPNS approach. Details of the TIPNS method are given in Ref. [40].

Grid generation

The grid was generated in two parts. First, the Roberts stretching transformation [47] was used to generate a highly refined grid near the wall. The stretching was dependent on the spacing of the first point off the wall y_{wall}, the total height of the grid, and the number of points in the normal y direction. The refinement in the y direction was maintained until the approximate edge of the boundary layer. Although the boundary-layer edge was defined in a very crude manner, it was found to be sufficiently accurate for the purposes of grid generation. A much coarser constant grid spacing was used away from the boundary layer, with care being taken to capture the shock accurately.

4 FLOW MODELING

Turbulent flow

In a supersonic turbulent flow, the small but significant subsonic portion of the boundary layer results in an elliptic region wherein the flow information can be conveyed upstream. In the presence of any disturbance such as an impinging shock or a change in body geometry such as a compression or an expansion ramp, this elliptic portion of the turbulent boundary layer results in a region of "influence" within which the incoming flow is affected by the disturbance far ahead of the actual presence of the disturbance. This sets up an interaction of the flow causing the turbulent flow to be influenced by the history of the flow and making the flow essentially "non-equilibrium". The current research is aimed at accurately predicting the streamwise regions of influence in a two-dimensional turbulent supersonic boundary layer. To achieve this end, the simplest turbulence model which would accurately capture the essential features of the flow physics, while curtailing the additional complexity to a minimum, was sought. Therefore, simpler algebraic models were used to achieve turbulent closure, instead of the more complex one-equation or two-equation turbulence models commonly used to model turbulent flow,

Relaxation eddy viscosity model

The relaxation eddy viscosity model of Shang and Hankey [42], along with the Baldwin-Lomax algebraic model [48] was chosen to model the turbulent flow. It was found to accurately capture the extent of streamwise influence regions, and hence the additional computations required for the use of one-equation and two-equation models was determined to be unnecessary. This model is based on experimental observations that in a highly decelerated or accelerated turbulent flow, the Reynolds shear stress remains nearly frozen at its initial value while being

convected along streamlines and then exponentially approaches a new equilibrium state [42]. The model consists of a very simple algebraic relation between the equilibrium eddy viscosity and the Reynolds shear stress relaxation phenomenon. It is numerically easy to implement and requires just two input parameters : λ, a time-like length scale describing the exponential decay of the eddy viscosity distribution, and an initial streamwise location x_{relax}, at which the relaxation phenomenon is started. The main effect of the relaxation parameters is to utilize the upstream history in the calculation of the Reynolds stress tensor, thus departing from the equilibrium approximation of the algebraic models and making it a more accurate tool in the computation of turbulent flows with upstream influence.

The original model developed by Shang and Hankey consisted of the algebraic model of Cebeci-Smith [49], with the relaxation model being added to it, in order to incorporate the effects of the flow history. In the current study, the Cebeci-Smith model used by Shang and Hankey is replaced by the Baldwin-Lomax model. The Baldwin-Lomax model defines the eddy viscosity soley in terms of the easily calculable quantities like the vorticity, thus avoiding the need to compute the edge of the boundary layer. This makes the model more suitable for the current study, as it is difficult to establish a clear edge for the turbulent boundary layer in shock separated flows.

The relaxation eddy viscosity model consists of a very simple algebraic relation for the *non-equilibrium* turbulent eddy viscosity and is given by

$$\mu_T = \mu_{T_0} + (\mu_{T_{eq}} - \mu_{T_0}) \left[1 - e^{-(\frac{\Delta x}{\lambda})}\right] \tag{4.1}$$

where μ_T is the relaxation turbulent eddy viscosity.

The local equilibrium value of eddy viscosity $\mu_{T_{eq}}$ and the equilibrium eddy viscosity μ_{T_0} at a reference location are generated using the algebraic Baldwin-Lomax model. In Eq. (4.1), the two input parameters are Δx, the distance between an initial station at which relaxation was initiated and the current station, and λ the relaxation length scale. Computational details of these parameters are explained in the following sections.

Equilibrium eddy viscosity $\mu_{T_{eq}}$

As mentioned previously, the equilibrium eddy viscosity is computed using the Baldwin-Lomax model [36], using the following equations.

$$\mu_T = \begin{cases} \mu_{T_i}, & y \leq y_m \\ \mu_{T_o}, & y > y_m \end{cases} \tag{4.2}$$

where y_m is the smallest value of y for which $\mu_{T_i} = \mu_{T_o}$.

For the inner layer

$$\mu_{T_i} = \rho l_{mix}^2 |\omega| \tag{4.3}$$

$$l_{mix} = \kappa y \left[1 - e^{(-y^+/A_o^+)}\right] \tag{4.4}$$

For the outer layer

$$\mu_{T_o} = \rho \alpha C_{cp} F_{wake} F_{kleb}\left(y; y_{max}/C_{kleb}\right) \tag{4.5}$$

$$F_{wake} = min\left[y_{max} F_{max}; C_{wk} y_{max} u_{dif}^2 / F_{max}\right] \tag{4.6}$$

$$F_{max} = \frac{1}{\kappa}\left[\max_y (l_{mix}|\omega|)\right] \tag{4.7}$$

where y_{max} is the value of y at which $l_{mix}|\omega|$ achieves its maximum value, $|\omega|$ is the magnitude of the vorticity vector and F_{kleb} is the Klebanoff intermittency function. The intermittency function is based on the findings of Klebanoff [36] that in the boundary layer, the flow is not always turbulent, but intermittently laminar and turbulent. The standard closure coefficients for the Baldwin-Lomax model [36] provide the required closure.

Streamwise start of relaxation x_{relax}

The eddy viscosity at an upstream location where the relaxation phenomenon is initiated, μ_{T_0}, is defined by selecting a reference location. For all the computed cases, this reference location was considered to have a fixed value given by

$$x_{relax} = x/L = 0.9027 \tag{4.8}$$

where L is the distance from the leading edge to the start of the compression ramp or expansion corner. In the present investigation, the effects of the variation of the initial location on the final solution were studied, and it was found that it did not have a noticeable influence on the overall solution, with no influence on the extent of influence of the shock separated turbulent boundary layer. This aspect of the relaxation model has been dealt with throughly in Ref. [17]. For all practical purposes, the streamwise location where relaxation is initiated can be considered a constant, leaving just one input parameter to be dealt with, namely the relaxation length scale. It can be shown that the upstream correlation function F which was developed in this study, is equivalent to the closure parameter x_{relax}. This provides a method to quantify the parameter x_{relax}, leaving just one turbulence closure parameter λ as a user specified parameter.

Relaxation length scale λ

The relaxation length scale λ is considered to be a measure of the memory of the stress-containing eddies [42]. It has been demonstrated by Bradshaw that this parameter is the ratio of the turbulent energy to the rate of production of the turbulent energy [42, 50]. In the current study λ is defined as

$$\begin{aligned} \lambda &= 5\delta_0 \quad for \quad compression \quad ramp \quad flows \\ \lambda &= 2\delta_0 \quad for \quad expansion \quad corner \quad flows \\ \lambda &= 20\delta_0 \quad for \quad shock \quad impingement \quad flows \end{aligned} \tag{4.9}$$

where δ_0 is the boundary-layer thickness of the flow at the location immediately upstream of the interaction region. The boundary-layer thickness was calculated using the numerical procedure given in Chapter 6. The present analysis confirmed the findings of Shang and Hankey [42] that although λ is thought to be a function of the y coordinate to account for the fact that turbulent eddies closer to the wall achieve equilibrium faster [50], there is no significant difference in the computed solution when λ is made a function of y.

An interesting by-product of the development of the upstream correlation function is that user specification of x_{relax} can be avoided. The upstream correlation function F (for compression ramp and expansion corner flows) predicts the streamwise start of upstream influence, and is consequently equivalent to the streamwise start of relaxation represented by the parameter x_{relax}. Hence, the streamwise start of relaxation x_{relax} can be calculated *a priori* as

$$x_{relax} = F\delta_L$$

where δ_L is the undisturbed boundary-layer thickness at L.

Transitional flow

Factors that trigger transition in supersonic flow are numerous. Among them are the freestream turbulence level, wall roughness, wall cooling and mass transfer. The most commonly used method to predict transition, linear stability analysis, assumes that the disturbances that cause transition in a flow are infinitesimal, and thus this method is unable to deal with flow perturbations of finite amplitude. Also, the mathematical complexity of this method increases tremendously when several flow parameters are considered. Hence, another approach was used in this study to predict the onset of transition.

It has previously been shown [52, 53, 54] that turbulence models in which the Reynolds stresses depend upon flow history can accurately predict the transition from laminar to turbulent flow for constant pressure gradient flows. It can be shown that the parameter k which represents the kinetic energy of the turbulent fluctuations, is proportional to the trace of the Reynolds stress tensor. Hence, an equation governing k can be used to compute transitional flow. In the current study, a two-equation model to predict transition was considered to be a good choice, as it is can be easily modified to include several of the factors that cause transition. This allows a detailed study of the affect of each of these factors on transition. The present research focuses on the affect of the freestream values of turbulence intensity Ti_∞, Mach number M_∞ and Reynolds number Re_∞ on the onset of transition.

The two-equation $k-\omega$ model [36] was chosen to model the transitional flow. Initially, a modified transitional $k-\omega$ model [53] was chosen as the most appropriate model for the

present research. This choice was based on the prior work that was done by Wilcox [53, 54], in predicting transition in subsonic flows. The transitional model is obtained by altering the closure constants of the basic $k-\omega$ model, thus theoretically enabling a more accurate prediction of the onset of transition. However, it was found that the Wilcox transitional model was both unreliable and inaccurate in predicting transition in two-dimensional supersonic flow. Hence, that approach was abandoned and the original two-equation $k-\omega$ model was used to compute the transitional flow.

Two-equation $k-\omega$ model

Two-equation models of turbulence, which provide equations for the computation of the eddy viscosity and a turbulence length scale, are considered to be "complete" [36] . The turbulent kinetic energy k equation is developed to incorporate the turbulent flow history in calculating the eddy viscosity. The specific dissipation rate ω equation is used to quantify the turbulent length scale. Specific dissipation rate ω is defined as the rate of dissipation of turbulent energy in unit volume and time, and has the dimensions of $time^{-1}$. The dimensions of ω, that of a frequency, indicate that it can be assumed to be an average frequency of the freestream turbulence.

Turbulence transport equations

The current research uses the two-equation $k-\omega$ turbulence model of Wilcox [36]. The governing equations for the turbulence model are

$$\frac{D\rho k}{Dt} = \tau_{ij}\frac{\delta u_i}{\delta x_j} - \beta^*\rho\omega k + \frac{\delta}{\delta x_j}\left[(\mu + \sigma_k\mu_t)\frac{\delta k}{\delta x_j}\right] \tag{4.10}$$

$$\frac{D\rho\omega}{Dt} = \alpha\frac{\omega}{k}\tau_{ij}\frac{\delta u_i}{\delta x_j} - \beta\rho\omega^2 + \frac{\delta}{\delta x_j}\left[(\mu + \sigma_\omega\mu_t)\frac{\delta\omega}{\delta x_j}\right] \tag{4.11}$$

The turbulent viscosity is computed using

$$\mu_t = \frac{\rho k}{\omega} \tag{4.12}$$

The notation for the closure coefficients in the above turbulence model, and their values are in accordance with Ref. [36]. The boundary condition for ω at a solid surface is

$$\omega = 10\frac{6\nu}{\beta\Delta y^2} \tag{4.13}$$

where Δy is the distance of the first point away from the wall. Only smooth adiabatic walls with no mass transfer have been considered in the present research.

Modifications for transitional flow

In order to predict transitional flow, it is necessary to have a mechanism to manipulate the onset of transition based on parameters that trigger transition. The parameters considered in the present study are Mach number M_∞, Reynolds number Re_∞ and freestream turbulence intensity Ti_∞. The freestream values of M_∞ and Re_∞ are input parameters to the solution of the supersonic flow, and can be varied easily. The $k-\omega$ model also requires input of the freestream values of k_∞, ω_∞ and μ_{t_∞}. In order to be able to trigger transition based on input values of Ti_∞, a relation between the freestream values of k_∞ and Ti_∞ in the transitional region is required. Based on Coles [21] experimental data, the relation was found to be

$$Ti_\infty = e^{14.37}{k_\infty}^{0.5} \tag{4.14}$$

Thus, using Eq. (4.14) the input value of k_∞ can be obtained based on the freestream value of Ti_∞. This provides a quick and easy method of studying the effect of freestream turbulence intensity on the flow at various Mach and Reynolds numbers in conventional wind tunnels. The freestream values of ω_∞ and μ_{t_∞} are given by

$$\omega_\infty = 10\frac{U_\infty}{L} \tag{4.15}$$

$$\mu_{t_\infty} = \frac{\rho_\infty k_\infty}{\omega_\infty} \tag{4.16}$$

5 TEST CASES

The PNS, IPNS and TIPNS algorithms have been demonstrated by Miller et al. [43, 46] to be accurate over the range of flow conditions that are considered in the present study. The accuracy of the $k-\omega$ model in computing transitional flow is demonstrated in this chapter. The accuracy with which the relaxation eddy viscosity model captures the streamwise regions of influence in a turbulent flow has been demonstrated in Ref. [18] and also in the current chapter.

Turbulent flow

The relaxation eddy viscosity turbulence model was used with the IPNS/TIPNS algorithm to compute the flowfields. The IPNS/TIPNS technique requires that the region where the algorithm iterates the solution to be specified beforehand. The rest of the flow is computed by the single-sweep space marching technique [40, 46]. This a priori specification was done in such a way that the iterative region encompassed the streamwise influence region. To ensure the independence of the computed solution on the specification of the region of iteration, computations were made varying the extent of the iteration region and no practical difference was found between the solutions.

The test cases presented here are three of the over 133 numerically computed compression ramp and expansion corner flowfields that were used to obtain the correlation functions. The test cases for the shock impingement flowfields have previously been presented in Ref. [17, 18]. The compression ramp test cases presented correspond to the experiments performed by Law [9], Settles et al. [6] and Zheltovodov [5]. Comparisons were also made with the OVERFLOW Navier-Stokes code [55] and the Navier-Stokes calculations of Shang and Hankey [41, 42].

For the compression ramp, comparison has also been made with the LES results of Urbin and Knight [56]. Comparisons with Shang and Hankey's skin-friction results are not made because their results are not grid-independent. The expansion corner test case corresponds to the experiment of Chung [13]. The computed solutions were subjected to a series of grid refinement studies and the first grid point above the wall was moved closer until it did not have any noticeable affect on the solution. of Chung [13].

Case 1: Compression ramp ($\theta = 15.0°$)

The flow parameters for this adiabatic wall compression ramp test case, which correspond to the experiments of Law [9], are

$$M_\infty = 2.96, \quad Re = 3.94 \times 10^7/m, \quad T_\infty = 98.91$$

The grid-independent results for pressure and skin friction are plotted in Figs. 5.1 and 5.2. The present results are compared with Navier-Stokes results and also with the experimental results of Law. It can be seen that the values of the computed pressure (see Fig. 5.1) using the present relaxation model are in good agreement with the experimental data points obtained by Law throughout the flowfield. A small difference exists in the region of the separated flow, but as the current study is concerned with only the streamwise extent of influence, and not in capturing all the details of the turbulent flow, this deviation was not considered significant. For this test case, it was found that using a smaller value for the turbulence closure parameter λ results in better agreement with the experimental pressure data. This is demonstrated in Fig. 5.1. A value of $\lambda = 2.0\delta_0$ was found to give the best agreement for the pressure data. As a skin friction criterion is used to predict the upstream influence length, the effect of λ variation on the wall pressure was not considered to be very important.

The skin friction results given in Figure 5.2, are in good agreement with the numerical results from the OVERFLOW Navier-Stokes code in the region leading to separation and in the separated region of the flow. From the figure, it is seen that the variation of λ does not have a significant effect on the upstream influence region. The skin-friction plot reveals some differences in the downstream region of flow, after re-attachment. However, as the criteria for

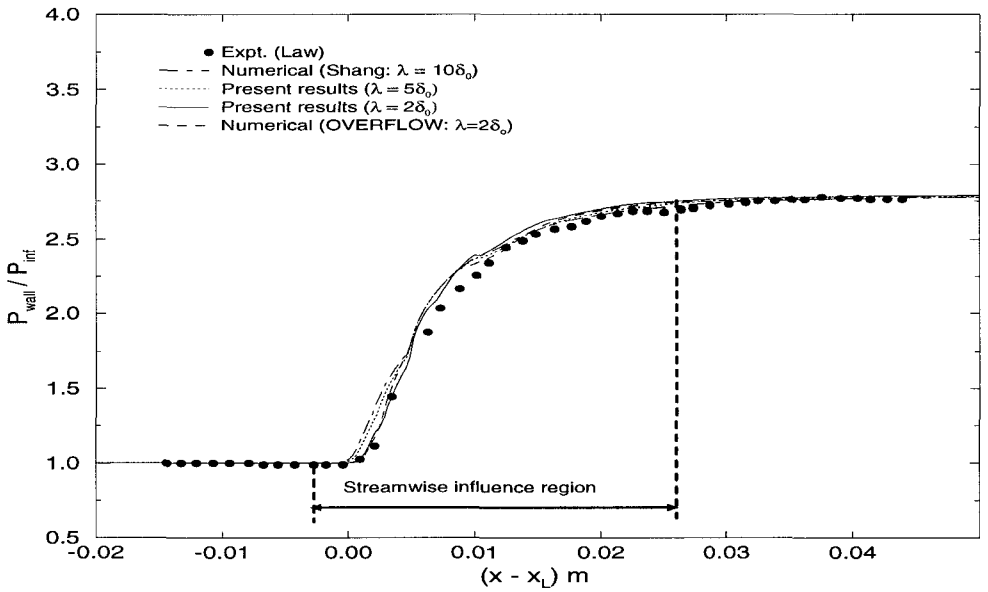

Figure 5.1 Wall pressure results for compression ramp case ($\theta = 15.0°$)

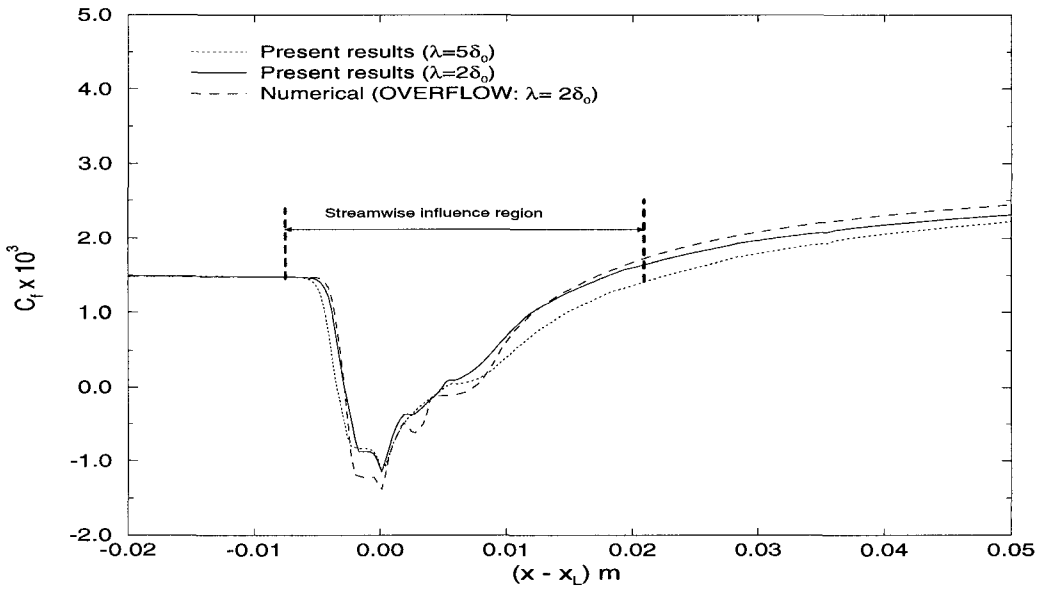

Figure 5.2 Skin friction results for compression ramp case ($\theta = 15.0°$)

the end of downstream influence was based on the values of wall pressure, this difference is not considered to be important, as it concerns the details of the turbulent flow and not the extent of influence of the shock separated flow.

In order to ensure that the developed correlations did not depend on the relaxation model closure parameters, x_{relax} and λ, a detailed study was carried out for a wide range of x_{relax} and λ values. It was determined that variation of x_{relax} and λ had no significant effect on predicting the start or the end of the streamwise influence regions. Details of the study are presented in Ref. [17].

Case 2: Compression ramp ($\theta = 17.0°$)

The inviscid pressure rise for this test case is

$$\frac{\Delta p}{p_\infty} = 2.135$$

while the other flow conditions are the same as in Test Case 1. The grid-independent results for pressure and skin friction are presented in Figs. 5.3 and 5.4. The same trends were noticed with this case as with Test Case 1. That is, the computed pressure plot can be seen to be in good agreement with the experimental data and the skin friction results are in good agreement in the region leading to separation and in the separated region of the flow, but differences exist in the downstream region. This agreement of upstream and downstream results is evident for both the numerical [55] and experimental [9] approaches. Therefore, applying the same reasoning as in Test Case 1, it can be concluded that the turbulent relaxation eddy viscosity model and the TIPNS algorithm used in the current study gives good results in the upstream region, and performs adequately in the downstream region.

Case 3: Compression ramp ($\theta = 8.0°$)

For this test case, comparison was made with two sets of experimental data, i.e, Settles et al. [6] and Zheltovodov [5]. The flow parameters for the Settles et al. [6] adiabatic wall compression ramp case are

$$M_\infty = 2.87, \quad Re = 6.3 \times 10^7/m, \quad (T_{stag})_\infty = 280$$

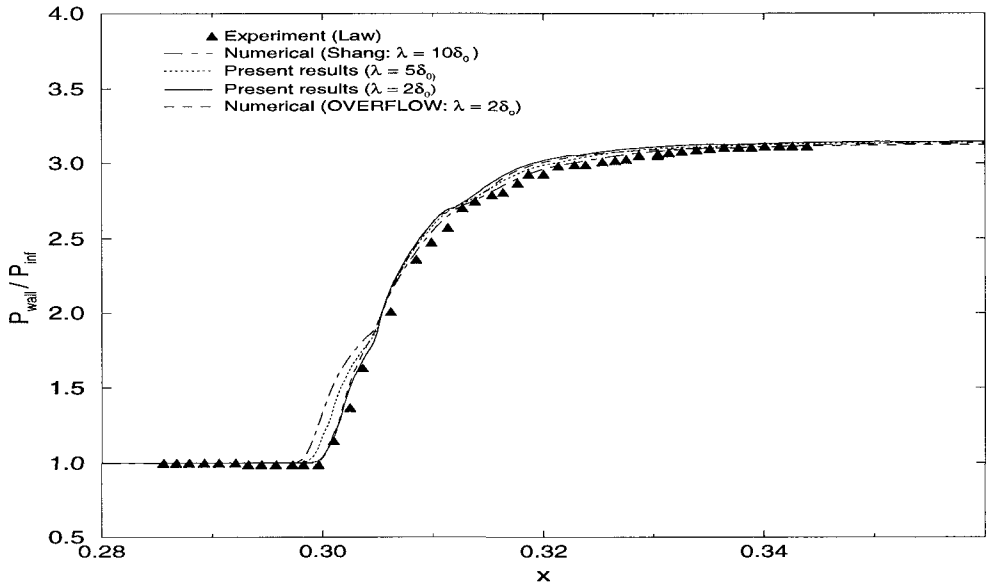

Figure 5.3 Wall pressure results for compression ramp case ($\theta = 17.0°$)

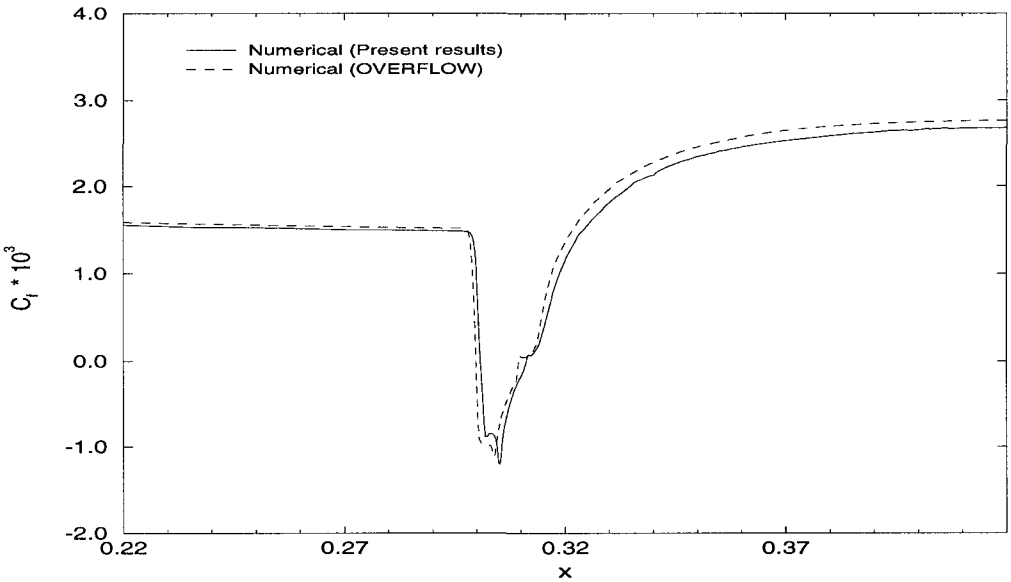

Figure 5.4 Skin friction results for compression ramp case ($\theta = 17.0°$)

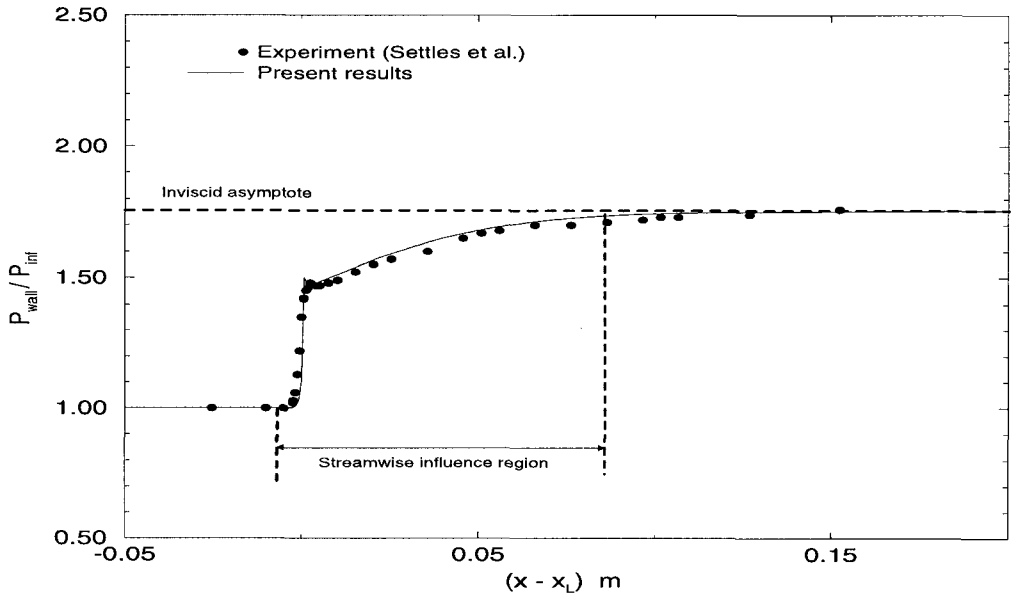

Figure 5.5 Wall pressure results for compression ramp case ($\theta = 8.0°$)

The results for wall pressure are presented in Fig. 5.5. During the computations, the computed boundary-layer thickness was matched to the experimental value of $\delta_0 = 2.6\ cm$ given in Ref. [6]. The computed pressure plot can be seen to be in good agreement with the experimental data.

The flow parameters for the Zheltovodov [5] adiabatic wall compression ramp case are

$$M_\infty = 2.95, \quad Re_{\delta_0} = 75 \times 10^3$$

The results for wall pressure are presented in Fig. 5.6, along with experimental data and the LES results from Ref. [56]. Again, a reasonable agreement is seen with both the experimental and LES results.

Case 4: Expansion corner ($\theta = -10.0°$)

The flow parameters for this adiabatic wall expansion corner case correspond to the experiment of Chung [13], and are given by

$$M_\infty = 1.28, \quad Re = 2.0 \times 10^7/m, \quad T_\infty = 98.91$$

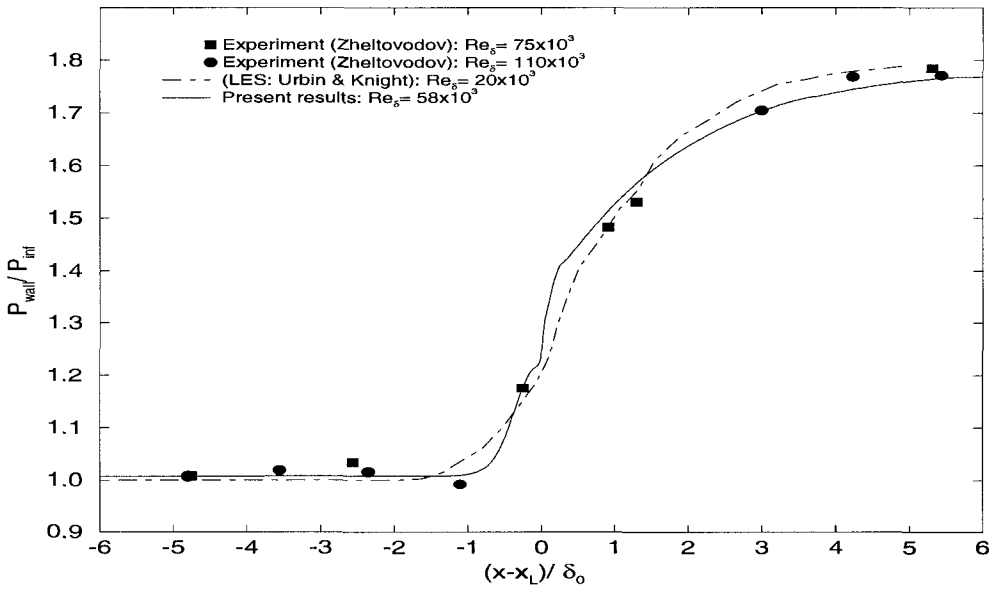

Figure 5.6 Wall pressure results for compression ramp case ($\theta = 8.0°$)

and the pressure drop is

$$\Delta p/p_\infty = 0.389$$

The grid-independent results for pressure are presented in Fig. 5.7. It can be seen that there is good agreement between the present results and the experimental data of Chung [13] throughout the flowfield. It should be noted, however, that the flow parameters of this experimental case are not in the valid range of the correlation functions developed for expansion corners. This case was used only to validate the accuracy of the TIPNS algorithm in computing expansion corner flowfields.

Transitional flow

To validate the model used for transitional flow, over 150 flat plate cases with differing flow parameters were computed, wherein values of M_∞, Re_∞ and Ti_∞ were varied. The test cases presented here are two of the over 150 cases that were computed. The two test cases correspond to the experiments conducted by Coles [21]. From Ref. [28], it was determined that

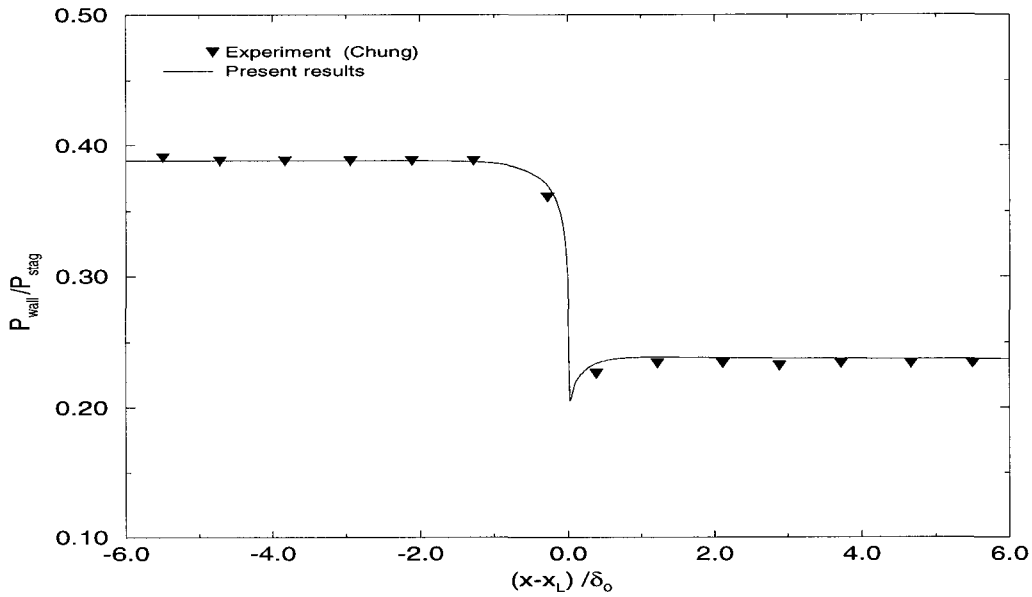

Figure 5.7 Wall pressure results for expansion corner case ($\theta = -10.0°$)

the turbulence levels in the JPL Wind tunnels where the experiments were conducted, were of the order of 1% at $M_\infty = 4.5$ with turbulent sidewall boundary layers. Laminar sidewall boundary layers reduced the turbulence level to 0.03%. The $k - \omega$ turbulence model was used with the space marching PNS algorithm. Comparisons were then made with the experimental data [21]. The computed solutions were subjected to a series of grid refinement studies where the first grid point above the wall was moved closer until it did not have any noticeable affect on the solution. An adiabatic wall boundary condition has been used for both the test cases. A reference temperature of $T_\infty = 273.31\ K$ is also used.

Case 5: Transition on a flat plate ($M_\infty = 2.57$)

The flow parameters for this flat plate test case are

$$Re_\infty = 1.14 \times 10^7/m$$

$$M_\infty = 2.57$$

$$Ti_\infty = 0.72\%$$

The results for the skin-friction coefficient are presented in Figure 5.8. The present results are compared with Coles experimental data. From Figure 5.8, it can be seen that the $k-\omega$ model accurately captures the onset of transition for this supersonic flat plate flow. Also the computed skin-friction plot is in good agreement with the experimental data points obtained by Coles over the entire transition region. The small difference near the maximum value of skin friction involves the details of transitional flow, and will not affect the prediction of the onset of transition. The Re_T value for this test case, using the minimum shearing stress criterion, is also in excellent agreement with the Re_T value obtained by Coles.

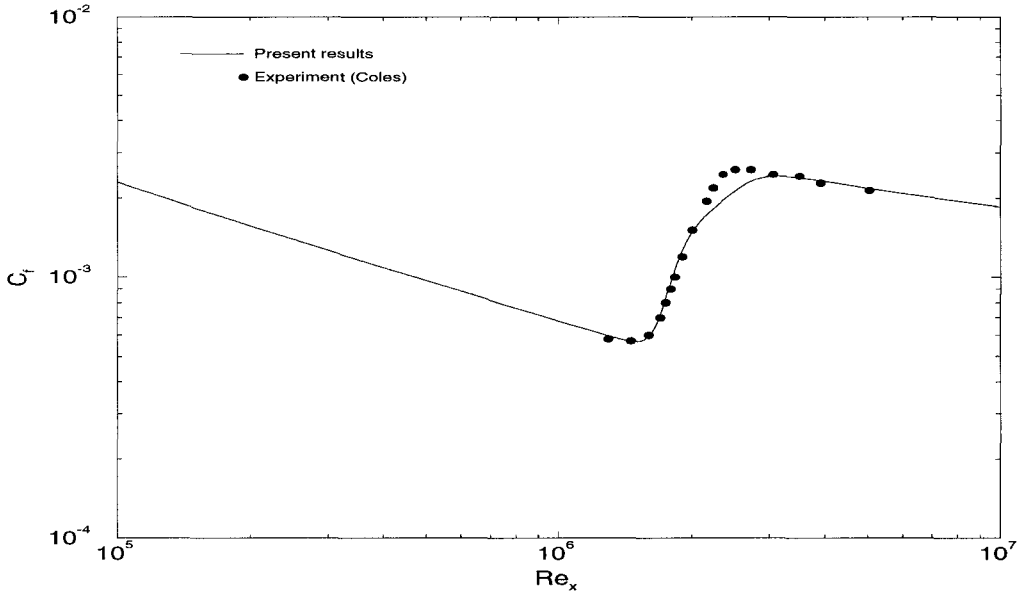

Figure 5.8 Comparison of skin-friction coefficient with experimental data at $M_\infty = 2.57$

Case 6: Transition on a flat plate ($M_\infty = 3.69$)

The flow parameters for this flat plate test case are

$$Re_\infty = 1.14 \times 10^7/m$$

$$M_\infty = 3.69$$

$$Ti_\infty = 0.83\%$$

The results for skin-friction coefficient are shown in Figure 5.9. The same trends that were noticed with Case 5 are also evident in this test case. That is, the computed skin-friction plot can be seen to be in good agreement with the experimental data through most of the transition region. Similarly, the small difference in results that is present in the region after the onset of transition will not affect the prediction of the onset of transition.

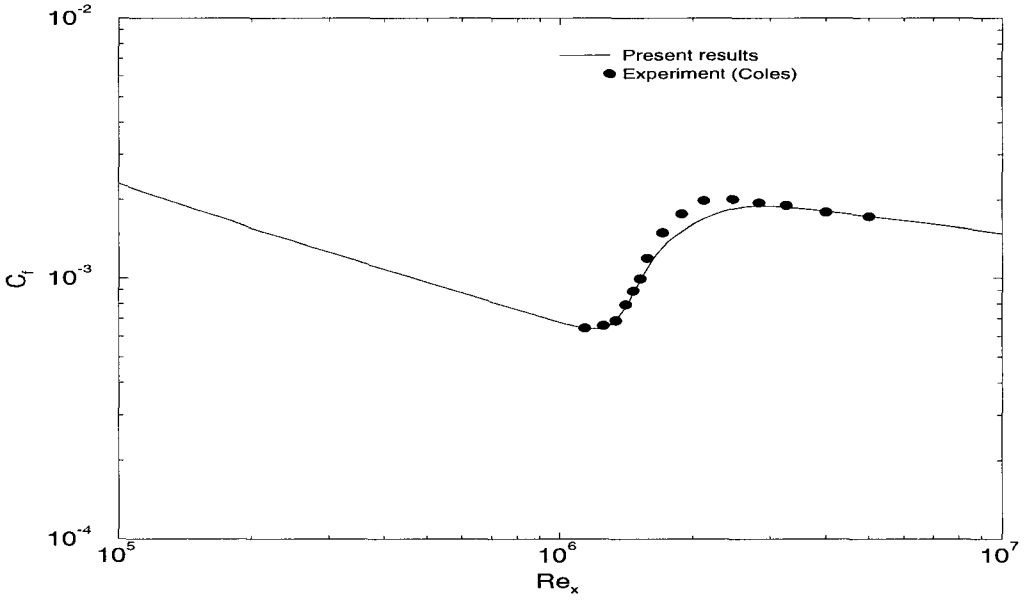

Figure 5.9 Comparison of skin-friction coefficient with experimental data at $M_\infty = 3.7$

6 CORRELATIONS TO PREDICT TURBULENT STREAMWISE INFLUENCE REGIONS

Using dimensional analysis, it can be shown that in a 2-D flow, the streamwise regions of influence should depend on the following flow parameters, namely, freestream Mach number (M_∞), freestream Reynolds number per unit length (Re), the magnitude of the overall pressure change $\Delta p/p_\infty$ (or the angle θ causing the pressure change) and the thickness of the undisturbed boundary layer δ_L. The dimensional analysis assumes an adiabatic wall boundary condition. The laminar and turbulent Prandtl numbers and the specific heat ratio are also assumed to be constant.

The various length scales used in the correlations for the case of flow over a compression ramp ($\theta > 0$) and an expansion corner ($\theta < 0$) are illustrated in Fig. 6.1.

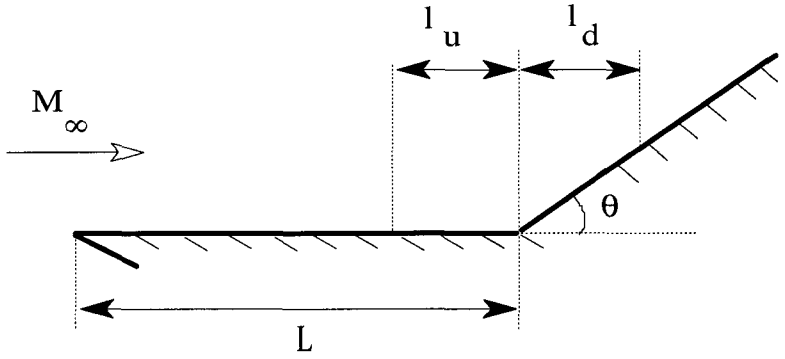

Figure 6.1 Length scales based on geometry

The upstream influence length is denoted by l_u and the downstream influence length by l_d. Also, l_u/δ_L is the upstream influence length ratio and l_d/δ_L is the downstream influence length ratio. Dimensional analysis then results in the following forms of the functions for the

lengths of the streamwise influence regions

$$\frac{l_u}{\delta_L} = F\left[Re, \frac{\delta_L}{L}, M_\infty, \frac{\Delta p}{p_\infty}\right] \tag{6.1}$$

$$\frac{l_d}{\delta_L} = G\left[Re, \frac{\delta_L}{L}, M_\infty, \frac{\Delta p}{p_\infty}\right] \tag{6.2}$$

A "boundary condition" of no influence in the absence of a disturbance, is applied to force the functions to follow the physics of the flow. i.e,

$$\left(\frac{l_u}{\delta_L} \to 0 \;\; and \;\; \frac{l_d}{\delta_L} \to 0\right) \;\; as \;\; \frac{\Delta p}{p_\infty} \to 0 \tag{6.3}$$

The TIPNS algorithm has been demonstrated by Miller et al. [40, 43] to be accurate over the range of flow conditions that are considered in the present study. The accuracy of the turbulent relaxation model in computing turbulent flows was demonstrated in Ref. [18] and also in the current study. Over 100 compression ramp cases and 33 expansion corner cases with differing flow parameters, i.e, different combinations of M_∞, Re and $\Delta p/p_\infty$ were computed using the TIPNS algorithm. Some of the grid-independent results from the compression corner calculations are presented in Table A.1 and the results from the expansion corner calculations are presented in Table A.2. Previously, 34 shock impingement cases were computed and their results were presented in Refs. [17, 18]. Regression analysis using the least squares approach was used to obtain the exponents of the flow parameters and to develop a final form for the correlations. The exponents for the flow parameters were obtained by cross plots of the flow variables. Further details of the procedure are given in Ref. [17].

To validate the numerically computed data points, experimental data was obtained from Refs. [9] - [15] and Refs. [41, 42, 48, 51]. The references, including the digital databases, generally provide the experimental data in the form plots of mean flow profiles, wall pressure and skin friction data. The start and end of the streamwise influence regions is not always quantified, i.e, a numerical value for l_u/δ_L and l_d/δ_L is not given for all experimental data. Therefore, some of the experimental data had to be deduced or extrapolated from the data presented by the authors.

Upstream correlation functions

In previous studies, the upstream influence length has been determined using either the "separation length" criterion or the "upstream pressure influence" criterion. The criterion of separation length is not suitable, as it assumes that only separated flows are being considered, whereas the current study considers both separated and attached flows. The upstream pressure influence criterion used by several experimental investigators is not conducive to numerical analysis. Hence, in the current study, the criterion used to obtain the upstream influence length was an engineering criterion rather than a theoretical one. The start of the upstream influence was defined as the x location at which the skin friction of the disturbed solution differed from the value obtained for the undisturbed flow over a flat plate by 1%. While recognizing that this is an *ad hoc* criterion, it should be noted that it provides an accurate numerical method of identifying the streamwise start of influence. With this criteria, the final form of the upstream correlation functions were found to be

Compression ramps

$$\frac{l_u}{\delta_L} = 48\frac{exp\ (0.1\ \theta + M_\infty^{0.3})}{(Re_{\delta_L})^{5/9}} \tag{6.4}$$

Expansion corners

$$\frac{l_u}{\delta_L} = 100\left[\frac{(\frac{|\Delta p|}{p_\infty})^{1/10}}{(M_\infty)^{9/10}(Re_{\delta_L})^{5/9}}\right] \tag{6.5}$$

Shock impingement

$$\frac{l_u}{\delta_L} = 273\left[\frac{(\frac{\Delta p}{p_\infty})^{4/3}}{(M_\infty)^{7/5}(Re_{\delta_L})^{1/3}}\right] \tag{6.6}$$

where Re_{δ_L} is the Reynolds number based on δ_L. The correlation functions along with the numerical and experimental data are plotted in Figs. 6.2 - 6.4.

For the case of a compression ramp (see Fig. 6.2), a comparison has been made with the upstream influence length obtained in various experiments [6]-[12]. The flow parameters in these experiments are within the valid range of the developed correlation function. From Fig. 6.2, it can be seen that the difference between the predicted and actual value of l_u/δ_L is significantly less than one boundary-layer thickness δ_L for all of the data, with a maximum

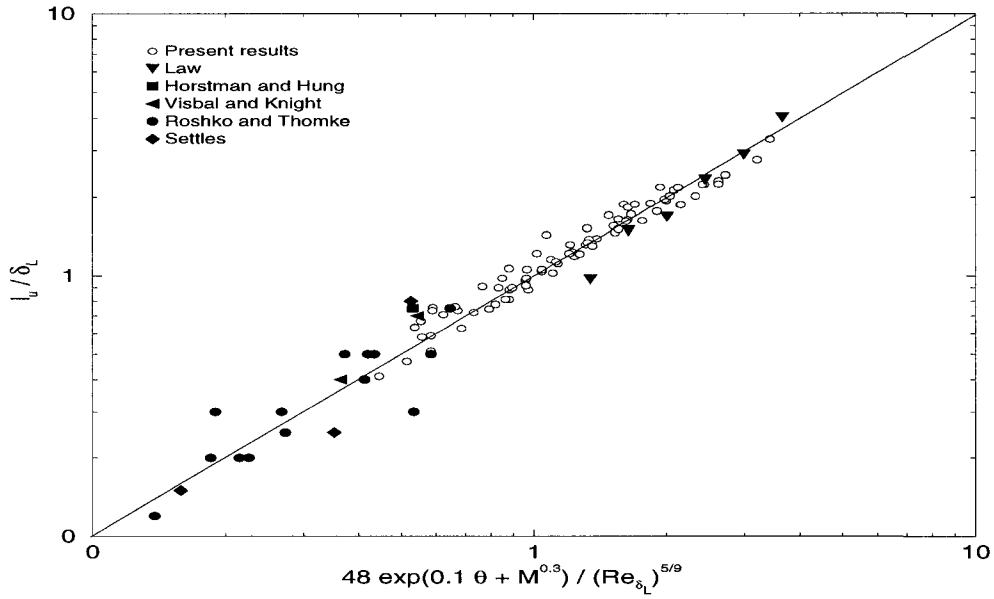

Figure 6.2 The upstream correlation function for compression ramps

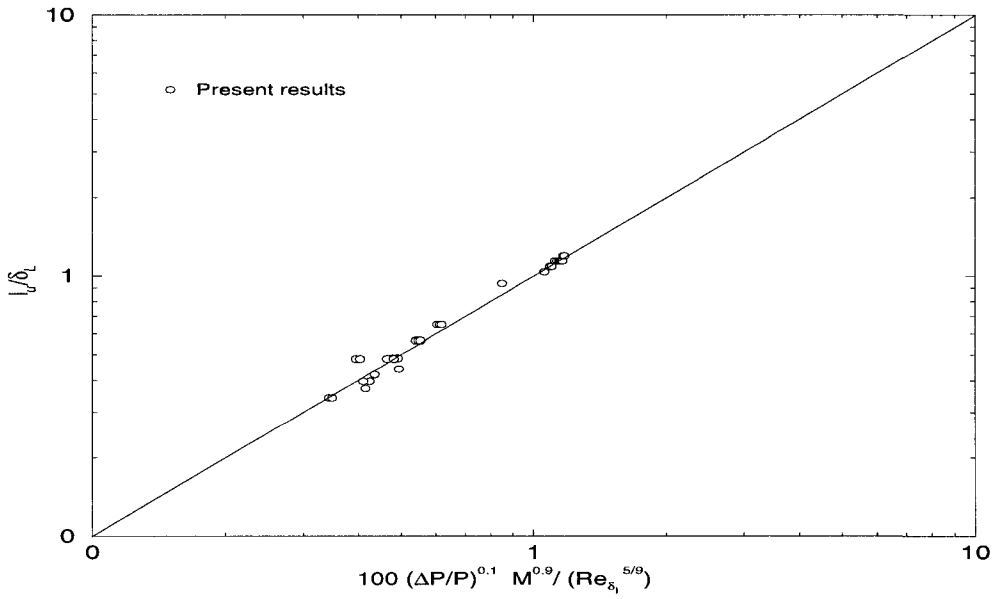

Figure 6.3 The upstream correlation function for expansion corners

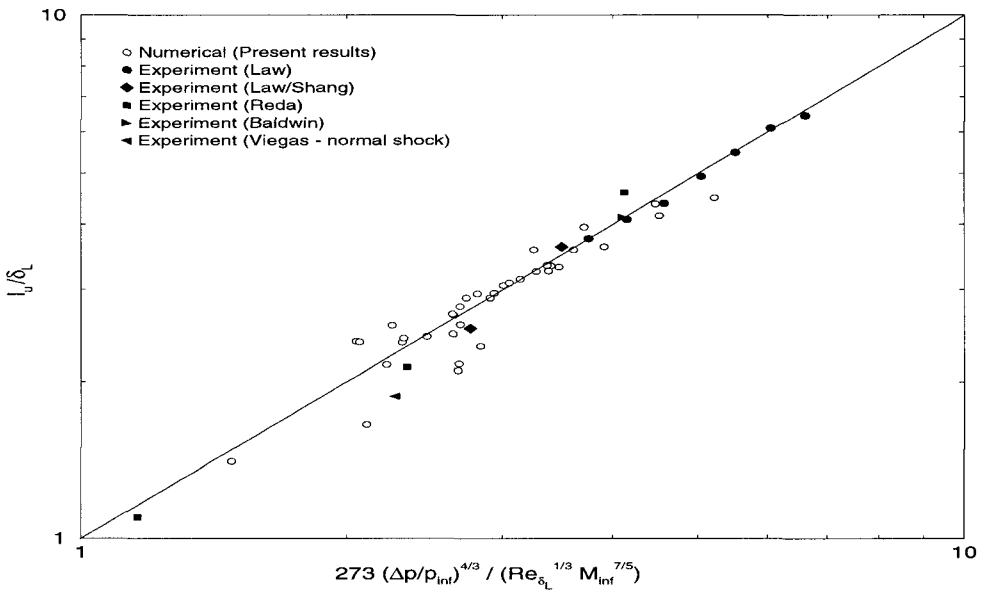

Figure 6.4 The upstream correlation function for shock impingement

difference of 0.32 δ_L. An exponential function was found to give the best fit for the data in the range considered for the case of a compression ramp, and hence the boundary condition of Eq. 6.3 was relaxed. An exponential scaling of the upstream influence was also presented by Settles et. al. [3], who developed the scaling of the upstream pressure influence parameter based on a surface pressure criterion. A comparison of the upstream influence length prediction using the experimental upstream pressure influence criterion results [12], and the skin friction criterion used in the current study is shown in Figure 6.5. The results are plotted for $Re_{\delta_0} \sim 1.3 \times 10^6$. It can be seen that the trend of the data is similar for both the criteria, with the present skin friction criterion predicting a larger upstream influence length.

For the case of an expansion corner (see Fig. 6.3), the numerical data obtained for the upstream influence length scaled well with the simple correlation developed. According to Narasimha and Sreenivasan [16] the interaction region for an expansion corner flow is insensitive to the corner deflection angle for low supersonic flows. This was corroborated in the current study where it was found that the upstream influence length l_u is independent of the corner deflection angle for fixed values of Mach and Reynolds numbers. The experimental results

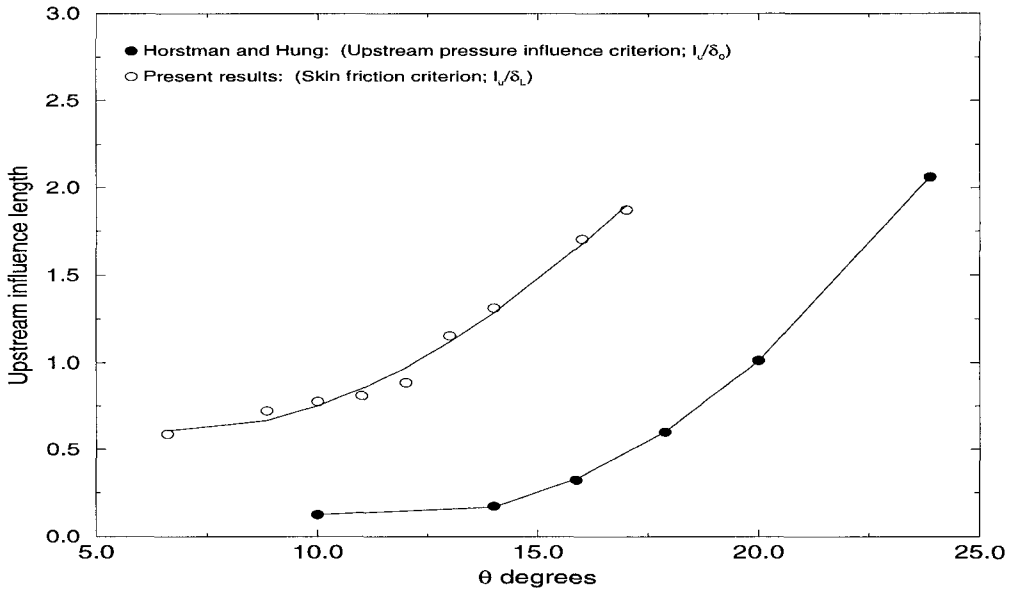

Figure 6.5 Comparison of criteria for upstream influence length for a compression ramp

from Refs. [13, 14, 15] did not include skin friction data, and hence could not be used for comparison with the upstream correlation function.

For shock impingement flows (see Fig. 6.4), comparisons have been made with the experimental data from Refs. [9, 42, 51, 48, 57, 58]. Further details regarding the development of the upstream correlation function for shock impingement flows are given in Refs. [17, 18].

From Figs. 6.2 - 6.4, it can be seen that the correlation functions accurately predict the extent of upstream influence for all the flowfields considered. It can be seen that the difference between the predicted and actual values of l_u/δ_L is significantly less than one boundary-layer thickness δ_L.

Downstream correlation functions

The criterion used to obtain l_d was also based on an engineering criterion. For compression ramps and shock impingement flowfields, the end of the downstream influence was defined as the x location at which the value of the pressure from the numerical solution differed from the

asymptotic value of the numerical solution by 1%. In the case of expansion corners, the end of the downstream influence was defined as the x location at which the value of the pressure from the numerical solution differed from the asymptotic value of the numerical solution by 5%.

The asymptote of the numerical solution was chosen instead of the inviscid asymptote in order to be consistent with the numerically computed solution. As the computed asymptote matches the inviscid asymptote, this was considered to be acceptable. The pressure criteria was employed to determine the downstream end of influence, as opposed to the skin friction criteria, since it was observed that downstream rise of skin friction is sensitive to the particular turbulence model employed and the parameters used for closure. This can also be observed in the literature [36, 51] when comparisons of different turbulence models are made. This made the choice of a pressure criteria more prudent, as the manner in which the pressure rises/drops to the inviscid asymptote is nearly independent of the relaxation parameters and turbulence models used. This provides an adequate method of identifying the streamwise end of influence.

Following the same method used for the upstream influence correlations, the downstream correlation functions were found to be

Compression ramps

$$\frac{l_d}{\delta_L} = \frac{0.5\ \theta\ (M_\infty)^{10/3}}{(Re_{\delta_L})^{1/3}} \tag{6.7}$$

Expansion corners

$$\frac{l_d}{\delta_L} = 2.2\ (\frac{|\ \Delta p\ |}{p_\infty})^{3/2} M_\infty^{9/5} \left[1 + \frac{1}{Re_{\delta_L}^{1/10}}\right] \tag{6.8}$$

Shock impingement

$$\frac{l_d}{\delta_L} = 3.3 \left[\frac{(\frac{3}{2}\frac{\Delta p}{p_\infty})(Re_{\delta_L})^{2/15}}{(M_\infty^{4/3}+1)}\right]^{0.75} \tag{6.9}$$

The downstream correlation functions are plotted in Figs. 6.6, 6.7 and 6.8. Comparison with accurate experimental data for all the downstream correlation functions could not be made, as the existing experimental data would have to be extrapolated to match the present criterion. However, in order to examine the trends of the correlations, some of the experimental data from Ref. [6] has been extrapolated for the compression ramp flowfield and plotted in

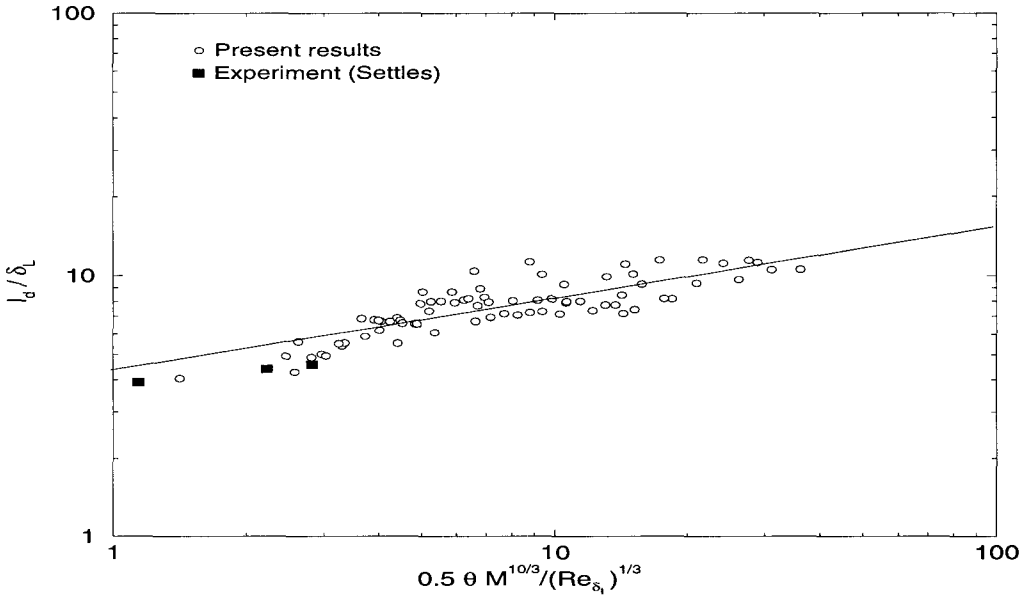

Figure 6.6 The downstream correlation function for compression ramps

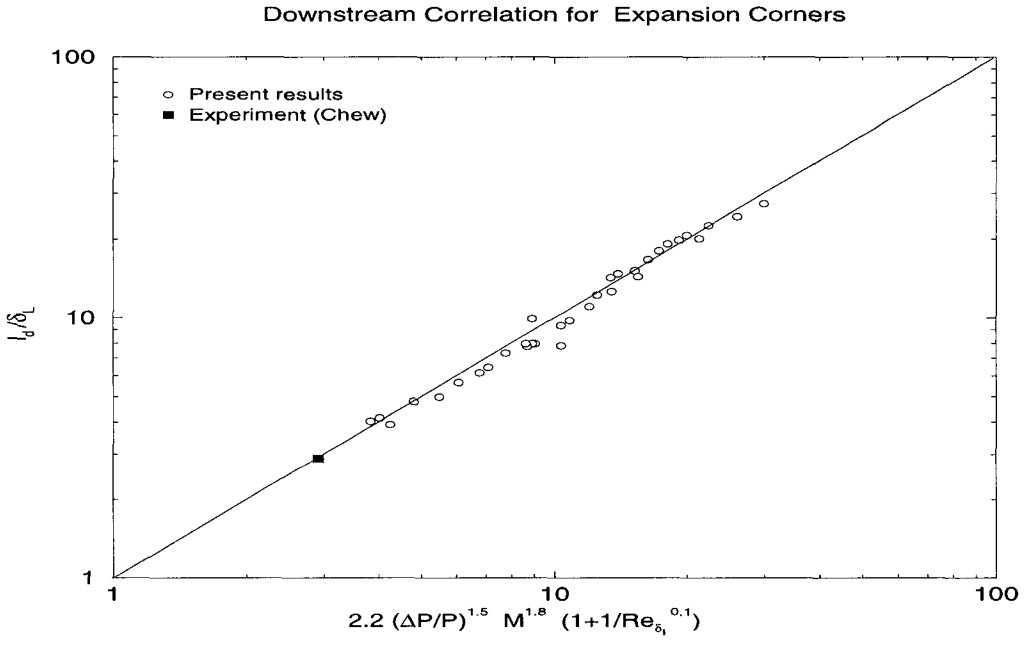

Figure 6.7 The downstream correlation function for expansion corners

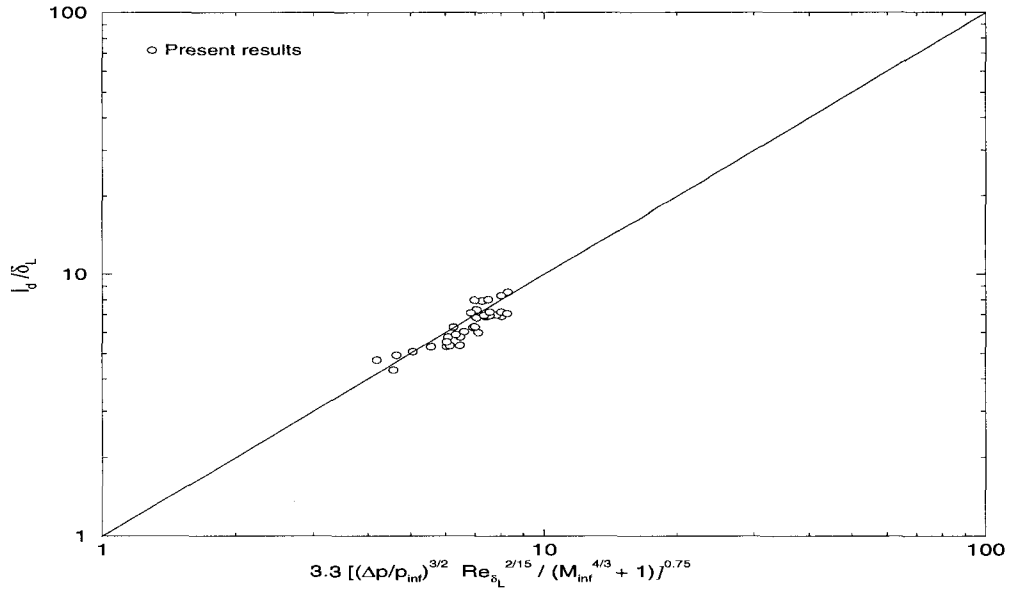

Figure 6.8 The downstream correlation function for shock impingement

Figure 6.6. It can be seen that the downstream correlation scales well with the extrapolated experimental data.

For the case of the expansion corner (see Fig. 6.7), the numerical data obtained for the downstream influence length scaled well with the simple correlation developed. A comparison of the downstream correlation function with the experimental data of Chew [15] is made. According to Lu and Chung [14], the downstream influence length of an expansion corner could be scaled with the hypersonic similarity parameter K . Figure 6.9 compares the results of the current downstream influence length with the scaling of Lu and Chung. In the current study, it was found that the downstream influence length l_d scales well to the hypersonic similarity parameter K based on the Mach number considered, with a distinct scaling for each Mach number.

The downstream correlation function for a shock impingement case is presented in Fig. 6.8. Further details regarding the development of the downstream correlation function for shock impingement flows are provided in Refs. [17, 18].

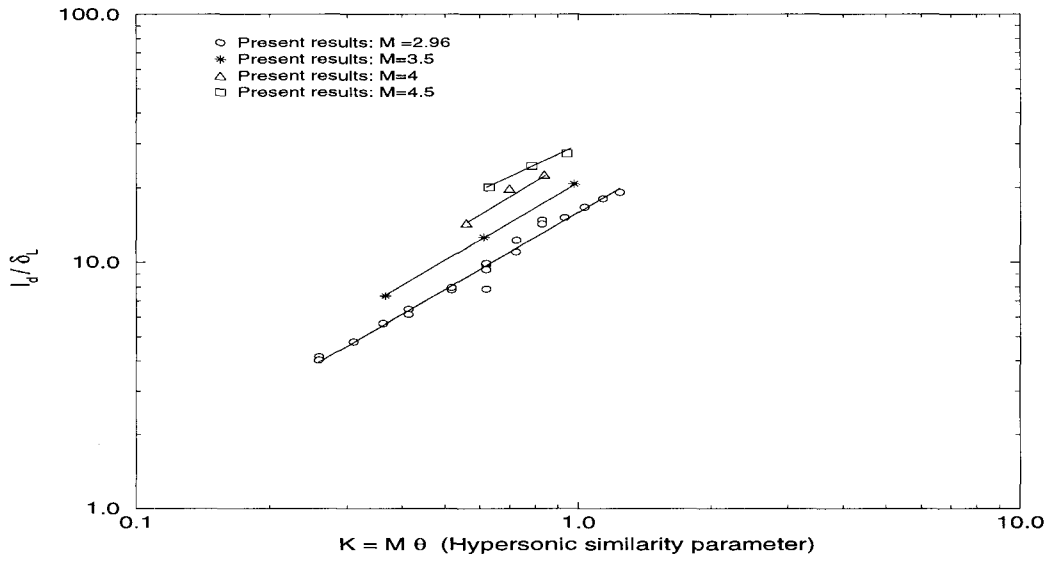

Figure 6.9 Comparison with expansion corner scaling of Lu and Chung

Range of validity of correlations

Both the upstream and downstream correlation functions have been found to be accurate over a wide range, as can been seen by the accuracy of these functions in scaling the experimental data points. The ranges of validity for the various flowfields are

Compression ramps

$$2.5 \leq M_\infty \leq 5.0$$

$$3.32 \times 10^6/m \leq Re \leq 1.11 \times 10^8/m$$

$$0.5 \leq \frac{\Delta p}{p_\infty} \leq 2.68$$

Expansion corners

$$2.5 \leq M_\infty \leq 4.5$$

$$3.3 \times 10^6/m \leq Re \leq 3.3 \times 10^7/m$$

$$0.328 \leq \frac{|\Delta p|}{p_\infty} \leq 0.895$$

Shock impingement

$$1.4 \leq M_\infty \leq 5.0$$

$$1.0 \times 10^6/m \leq Re \leq 1.0 \times 10^8/m$$

$$1.0 \leq \frac{\Delta p}{p_\infty} \leq 5.0$$

It should be noted that the correlation functions that have been presented so far, have been developed without any safety factor σ. For regions that have massive separation and also to take into account the vagaries of the present turbulence model, a safety factor of 10% is recommended for both the upstream and downstream correlation functions that have been developed.

The value of the compressible turbulent boundary-layer thickness δ_L required for the present correlations can be readily computed using a basic turbulent flow code. Alternatively, δ_L can be determined using an approximate empirical formula that was developed previously [18]. However, it should be noted that the values of δ_L used in the current study are the actual computed values obtained during calculations.

An interesting by-product of the development of the upstream correlation function is that user specification of the turbulence closure parameter x_{relax} can be avoided. The upstream correlation function F predicts the streamwise start of upstream influence, and is consequently equivalent to the streamwise start of relaxation represented by the parameter x_{relax}. Hence, the streamwise start of relaxation x_{relax} can be calculated *a priori* as

$$x_{relax} = F\delta_L$$

where δ_L is the undisturbed boundary-layer thickness at L. This equivalence implies that the arbitrary closure parameter x_{relax} of the relaxation model can be quantified using an empirical relation, namely F, leaving just one closure parameter λ as user specified.

7 CORRELATIONS TO PREDICT THE ONSET OF TRANSITION

Using dimensional analysis, it can be shown that in a supersonic 2-D flow over a smooth flat plate, the onset of transition should depend on the following flow parameters, namely, the freestream Mach number M_∞, the freestream Reynolds number per unit length Re_∞, the magnitude of the overall pressure change $\Delta p/p_\infty$ and the freestream turbulence intensity Ti_∞. The dimensional analysis assumes a smooth flat plate and an adiabatic wall boundary condition. The laminar and turbulent Prandtl numbers and the specific heat ratio are assumed to be constant. The focus of the current research is on flow past flat plates with a zero pressure gradient. Hence, the magnitude of the overall pressure change $\Delta p/p_\infty$ is not considered to be a parameter in determining the correlations, and is dropped from consideration. Figure 7.1 illustrates the location of the onset of transition in a supersonic flow. The location of the onset of transition is denoted by x_T and the Reynolds number at the start of transition is denoted by Re_T. Dimensional analysis then results in the following form of the function for the onset of transition

$$Re_T = G\left[Re_\infty, M_\infty, Ti_\infty\right] \tag{7.1}$$

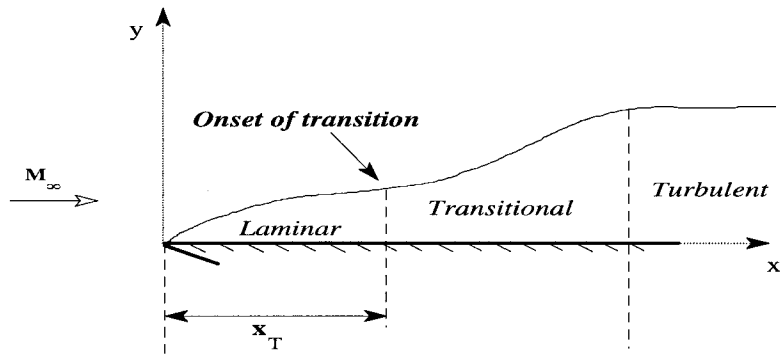

Figure 7.1 Onset of transition

Transition criteria

It is a well documented fact that the vagaries of wind tunnels make it difficult to reconcile the transition measurements in different wind tunnels. Therefore, for an empirically developed transition correlation to be valid, the criteria used in determining the onset of transition assumes an added significance. Some of the criteria that have been used to determine the onset of transition are based on the location of

- Minimum shearing stress
- Minimum static pressure
- $R_t = \frac{\mu_t}{\mu_t} > 1$ where R_t is the turbulent Reynolds number.

In the current study, all of the above mentioned criteria were considered and compared with the available experimental and numerical data. This was done in order to eliminate any possible errors based on the criterion in the correlations. However, the criteria using the value of shear stress is considered to be the most important, as minimum and maximum values of skin friction directly lead to the calculation of the drag over a body. Therefore, from the perspective of engineering applications for which the current research is intended to apply, the shearing stress criteria is considered the most pertinent. Hence, the correlation function was developed based on the minimum shearing stress criteria. Also, since the turbulent Reynolds number R_t criteria is geometry dependent, it was not considered to be a suitable criteria. Additionally, these correlations are developed based on conventional wind tunnel measurements, as opposed to quiet tunnel data. Currently, numerical difficulties prevent computation of the transitional flow at very low turbulence intensity levels, so that a direct comparison with the low noise/quiet wind tunnel data cannot be made.

Comparison of criteria

Different criteria to measure transition have been tested. A sample of the calculations for the onset of transition is presented in Table A.3. Figure 7.2 is a plot of the variation of

the transition Reynolds number at onset with unit Reynolds number. for both of the criteria considered. Figure 7.3 is a plot of the variation of the transition Reynolds number at onset with Mach number for different transition criteria is shown in Figure 7.3. Results are shown for various transition criteria. From Figure 7.2, it is evident that there is good agreement of the numerically computed transition Reynolds numbers with Coles experimental data.

As expected, from the plots, it is evident that the criterion used to predict transition plays an important role in determining the actual correlation function. However, the *trend* of the data is the same regardless of the criterion used.

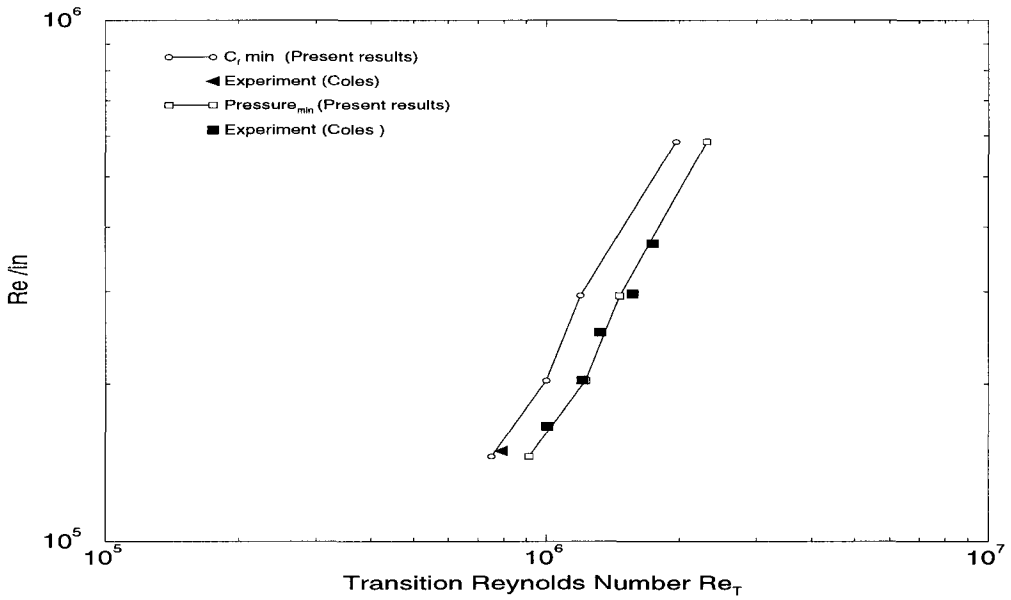

Figure 7.2 Onset of transition at $M_\infty = 3.7$ using different criteria

Effect of parameters on Re_T

From a literature survey of experimental, theoretical and empirical data, it was found that Re_T increases with both Reynolds number Re_∞ and Mach number M_∞. The influence of Ti_∞ on Re_T is more complex. Relations of the following form were expected

$$Re_T \sim {Re_\infty}^a$$

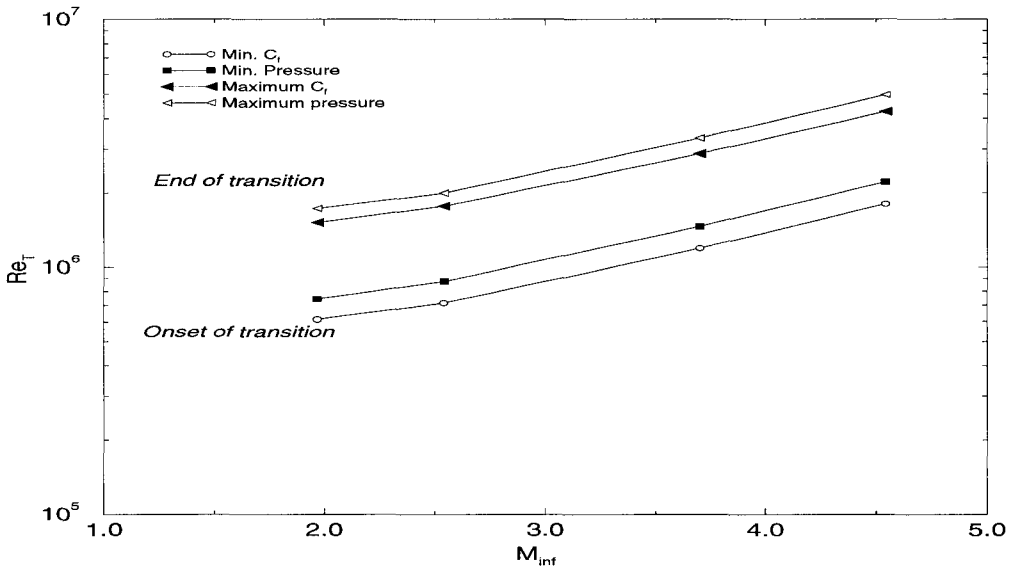

Figure 7.3 Onset of transition at $Re_\infty = 7.9e7$ using different criteria

$$Re_T \sim exp(b\ M_\infty)$$

$$Re_T \sim F(c\ Ti_\infty)^d$$

where *a, b, c and d* are any positive or negative fractions. Cross plots of the various transition parameters being considered are used to aid in the determination of the above functional relationships and the development of a comprehensive correlation function for onset prediction.

Effect of Reynolds number Re_∞

Cross plots of the transition Reynolds number Re_t with increasing Reynolds number for different M_∞ values are shown in Figures 7.4, 7.5 and 7.6 for two values of turbulence intensity Ti_∞.

The increase in Re_t with increasing Reynolds number has been obtained by previous investigators, for example Ref [21, 22, 24]. From the graphs, it can be seen that the slopes of the lines depend on M_∞ as well as Re_∞. Therefore, different forms of the exponent for the Reynolds number relation were investigated. Two of the functions are given below, with the

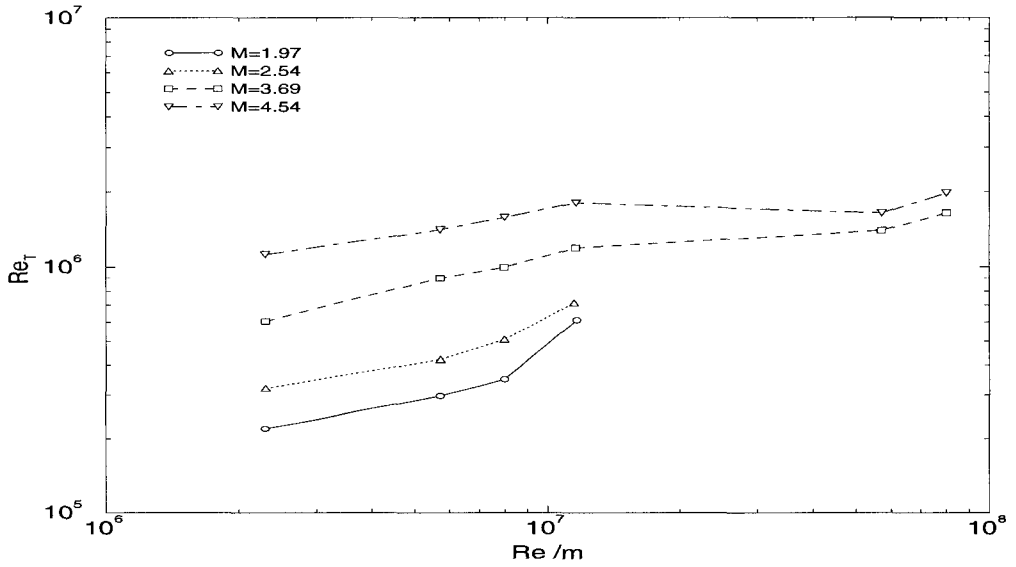

Figure 7.4 Variation of Re_T with Reynolds number for $Ti_\infty \sim 0.83\%$.

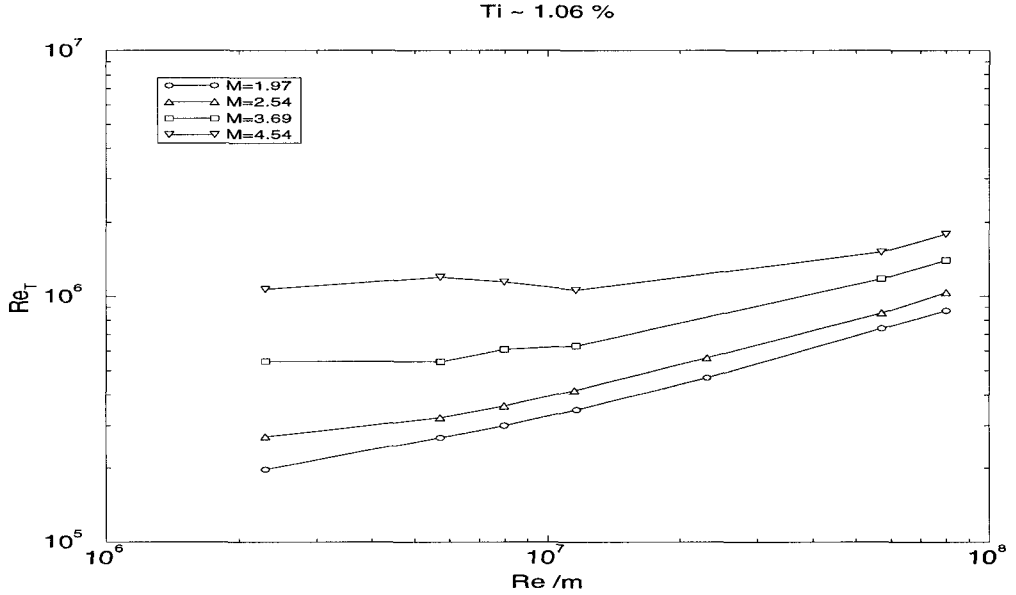

Figure 7.5 Variation of Re_T with Reynolds number for $Ti_\infty \sim 1.06\%$.

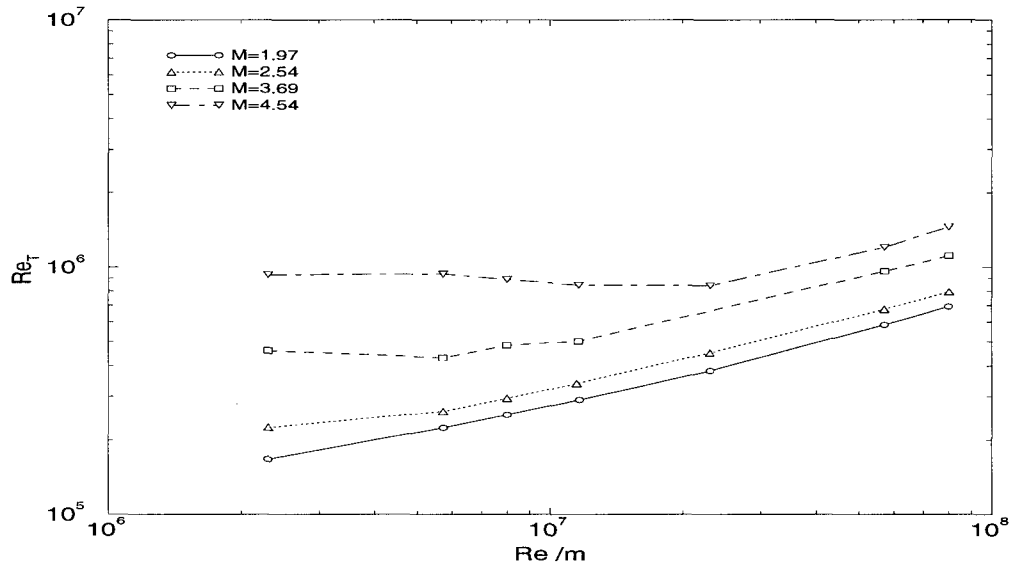

Figure 7.6 Variation of Re_T with Reynolds number for $Ti_\infty \sim 2.13\%$.

function involving M_∞ yielding a better fit.

$$Re_T \sim Re_\infty^{(0.66-0.11\ M_\infty)} \tag{7.2}$$

$$Re_T \sim Re_\infty^{0.285} \tag{7.3}$$

Experimental data and the trends of the Re_∞ variation obtained by previous investigators are plotted against the present results in Figure 7.2, which shows good agreement between the present results and previously reported trends. Figure 7.7 compares the trend of the current data with that obtained in a low-noise wind tunnel [22]. It can be seen that as the turbulence intensity decreases, the trend of the present data agrees well with that of the quiet tunnel data. It should be noted that an "abrupt rise in pressure" criterion was used to plot this graph.

Effect of Mach number M_∞

Cross plots of the transition Reynolds number Re_t with increasing Mach number for different Reynolds number are shown in Figures 7.8, 7.9 and and 7.10. The value of turbulence intensity Ti_∞ is varied as well.

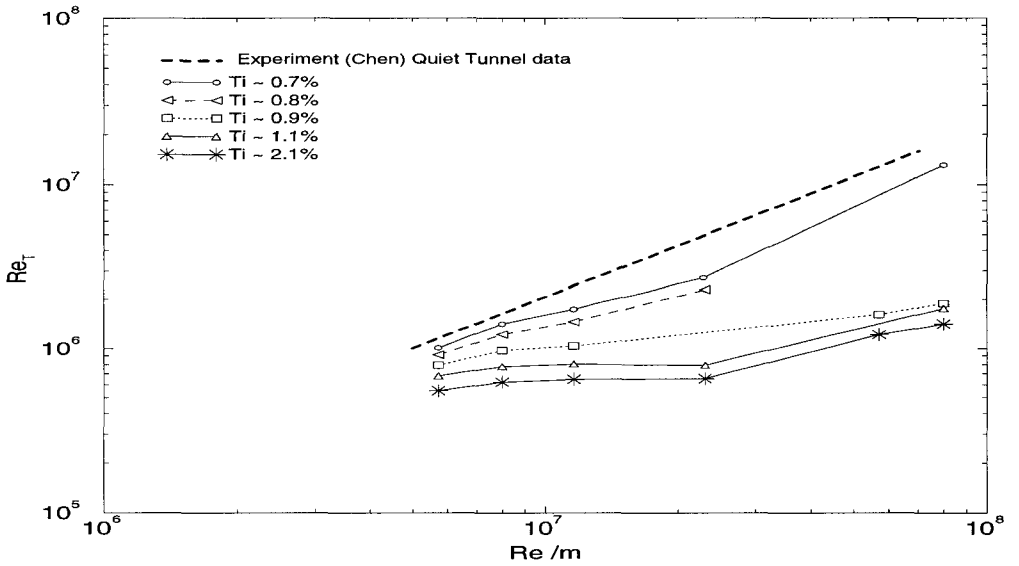

Figure 7.7 Comparison of Re_T trend with quiet tunnel trend.

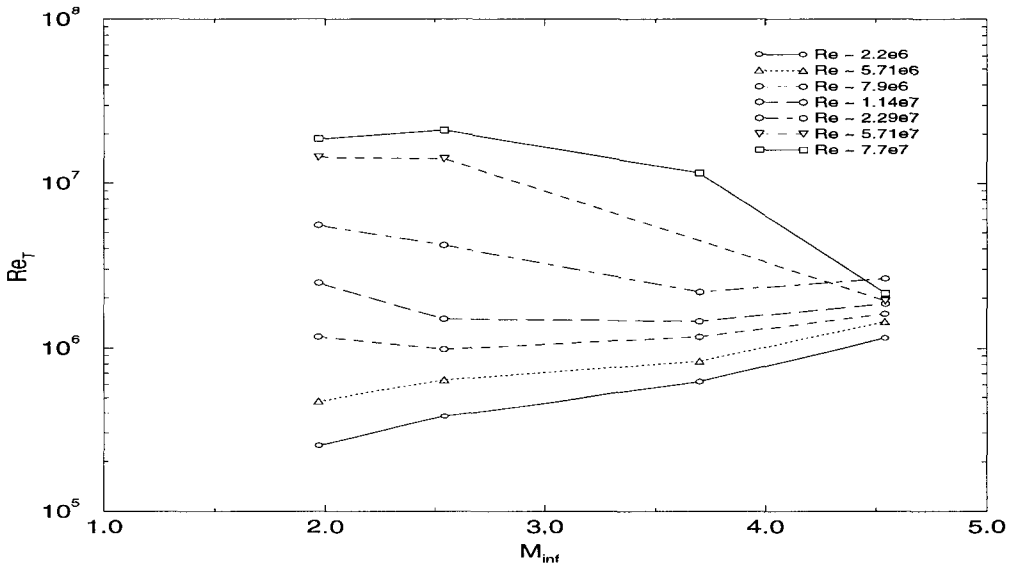

Figure 7.8 Variation of Re_T with Mach number for $Ti_\infty \sim 0.7\%$.

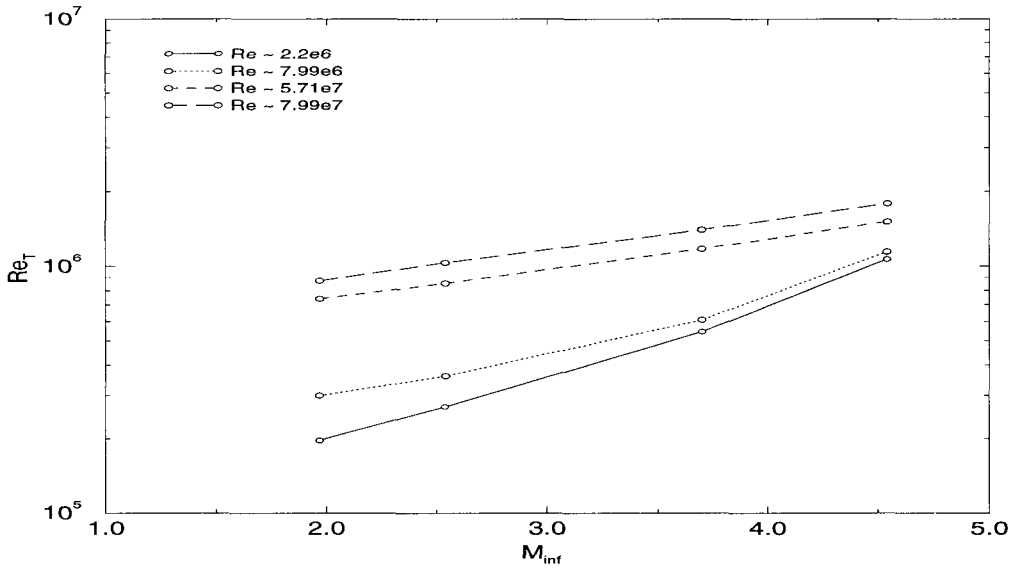

Figure 7.9 Variation of Re_T with Mach number for $Ti_\infty \sim 1.1\%$.

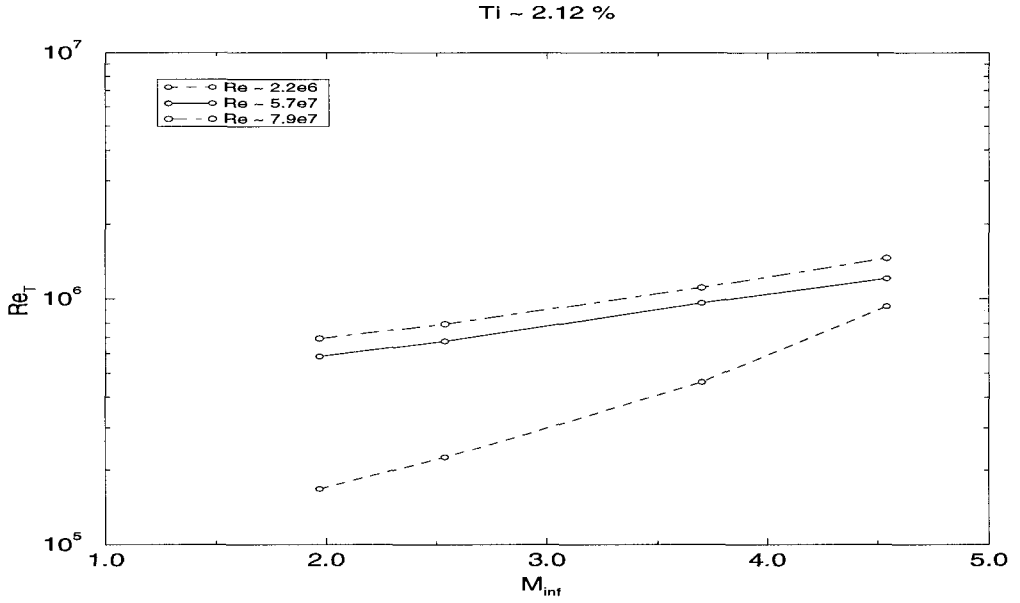

Figure 7.10 Variation of Re_T with Mach number for $Ti_\infty \sim 2.12\%$.

The increase in Re_t with increasing Mach number has been shown by previous investigators, for example, Ref. [24, 25]. Figure 7.11 compares the hollow-cylinder data from Ref. [24] with the present flat plate results for different Mach numbers. It should be noted that in Ref. [25], questions are raised regarding the comparison of the Mach number trends of transition data in conventional wind tunnels, due to the influence of radiated aerodynamic noise. However, in the present study, there was noticed a definite increase in Re_t with M_∞, for the lower Reynolds numbers, and a slight leveling off of the trend for the low turbulence intensity, high Reynolds number data. As noted previously, it can be seen that the exponent of the function varies with all the parameters considered, i.e, M_∞, Ti_∞ and Re_∞.

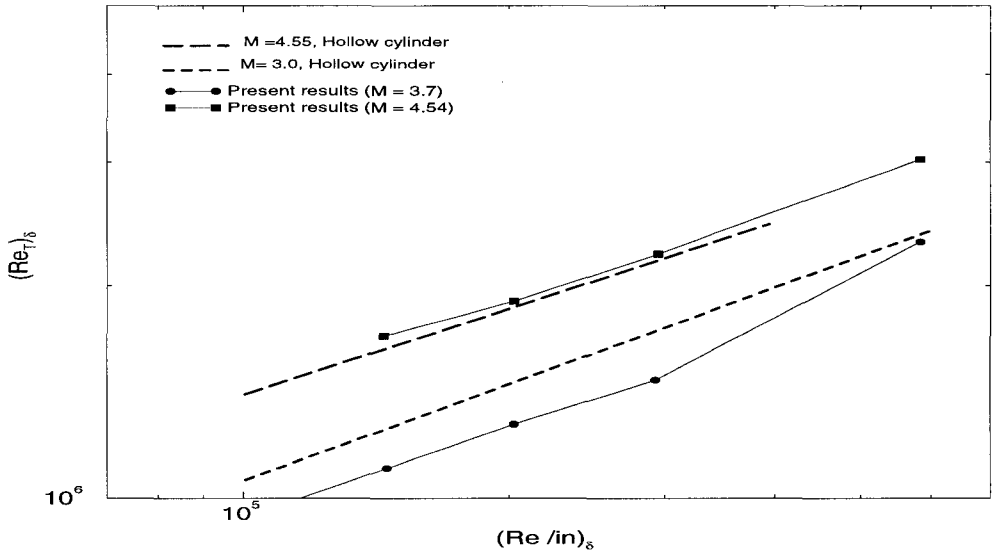

Figure 7.11 Comparison of Mach number trends with increasing Reynolds number.

Effect of turbulence intensity Ti_∞

Cross plots of the transition Reynolds number Re_T with increasing Ti_∞ are shown in Figures 7.12 and 7.13 for various Mach and Reynolds numbers. The effect of Ti_∞ on the Mach number and Reynolds number can also been seen from Figures (7.4 - 7.9). From the graphs, it is apparent that the variation of Ti_∞ gives rise to a complex function, as there exists a

significant interdependence of Mach number, Reynolds number and Ti_∞.

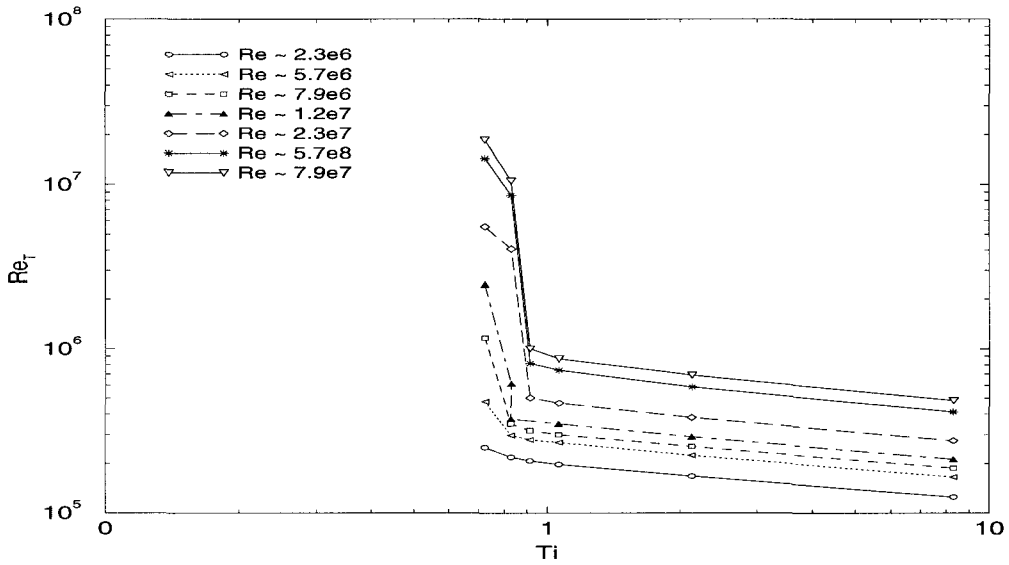

Figure 7.12 Variation of Re_T with Reynolds number for $M = 1.97$.

Final form of correlation

Difficulties were encountered while combining the effects of variation of all the flow parameters, in order to obtain a comprehensive correlation function to predict the onset of transition. The main obstacle to developing a single correlation function was the change in the trend of Ti_∞ as the values of Ti_∞ increase above 0.9%. It should also be noted that this change in the trend of Ti_∞ has not been reported in the literature. It was found that the data involving the variation of Ti_∞ is not readily amenable to developing a comprehensive correlation function which spans the entire range of turbulence intensities considered. Hence a specific correlation for each value of Ti_∞ was sought. The correlation function obtained is given by

$$Re_T = b\, G^m \tag{7.4}$$

where

$$G = \frac{e^{(2.15\ M_\infty)} Re_\infty^{(0.66-0.11\ M_\infty)}}{(2 - exp(-Ti))} \tag{7.5}$$

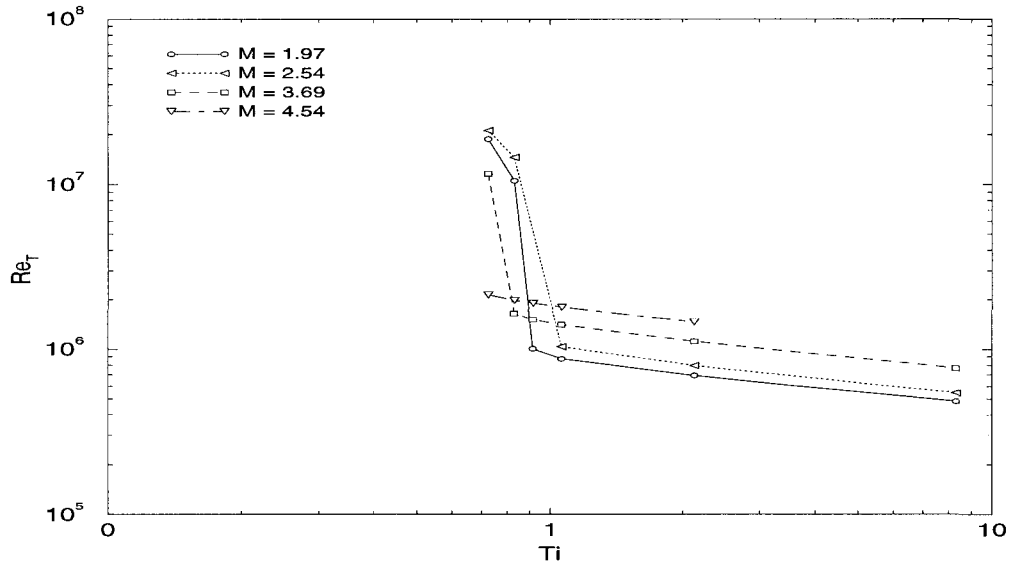

Figure 7.13 Variation of Re_T with Mach number for $Re_\infty = 7.9e7$.

In developing this function, the parameters m and b were found to be positive numbers that vary according to the turbulence intensity. The values of m and b for each Ti_∞ value considered are given in the Table A.4. From the table, it is evident that the value of m, the slope of the correlation function, can be assumed to be a constant value of 1.1. However, the value of b is a more complex function of Ti_∞, and is an obstacle to developing a comprehensive correlation function for the entire range of Ti_∞ values considered. Figure 7.14 graphs the variation of b with respect to Ti_∞. Though the value of b is a complex function of the turbulence intensity, a value for intermediate values of Ti_∞ can be easily obtained by interpolating the data from the figure. Hence, the final form of the correlation function obtained is given by

$$Re_T = b \left[\frac{e^{(2.15\ M_\infty)} Re_\infty^{(0.66-0.11\ M_\infty)}}{(2 - exp(-Ti))} \right]^{1.1} \tag{7.6}$$

where the values of b are given in Table A.4. The graphs of the individual functions are plotted in Figures 7.15 - 7.20. Figure 7.21 compares the correlation functions for all the values of Ti_∞ considered in this study.

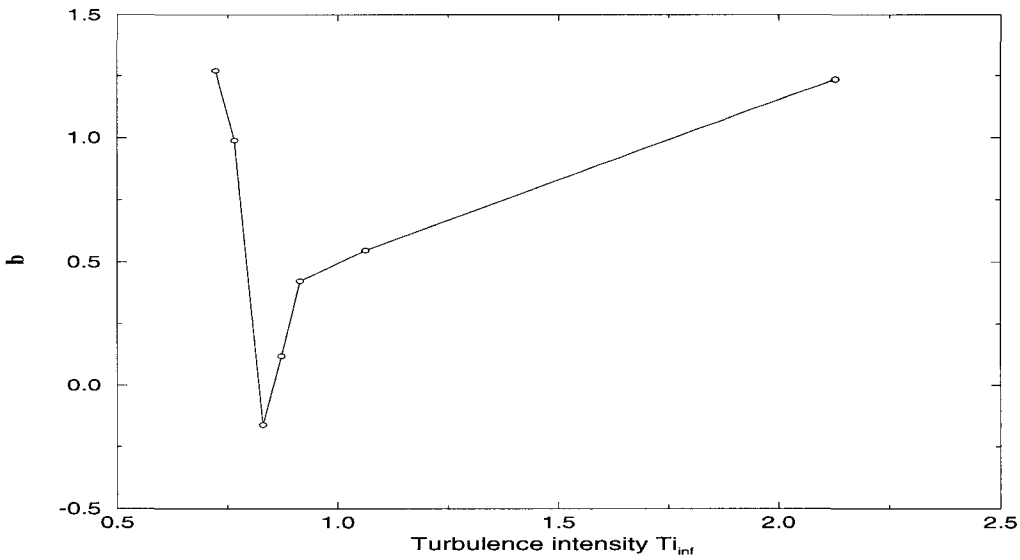

Figure 7.14 Variation of b with Ti_∞

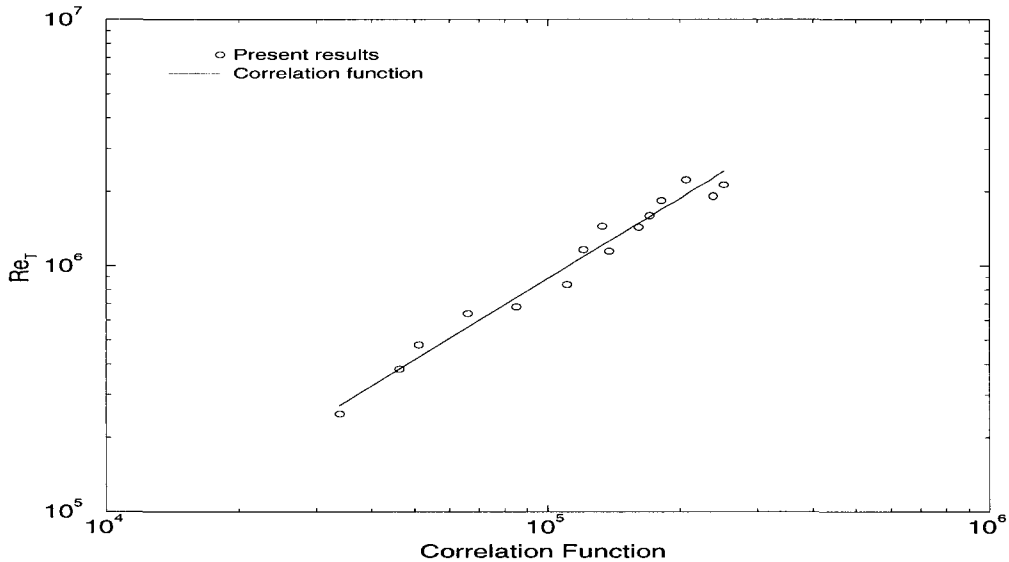

Figure 7.15 Correlation function for $Ti_\infty = 0.7\%$

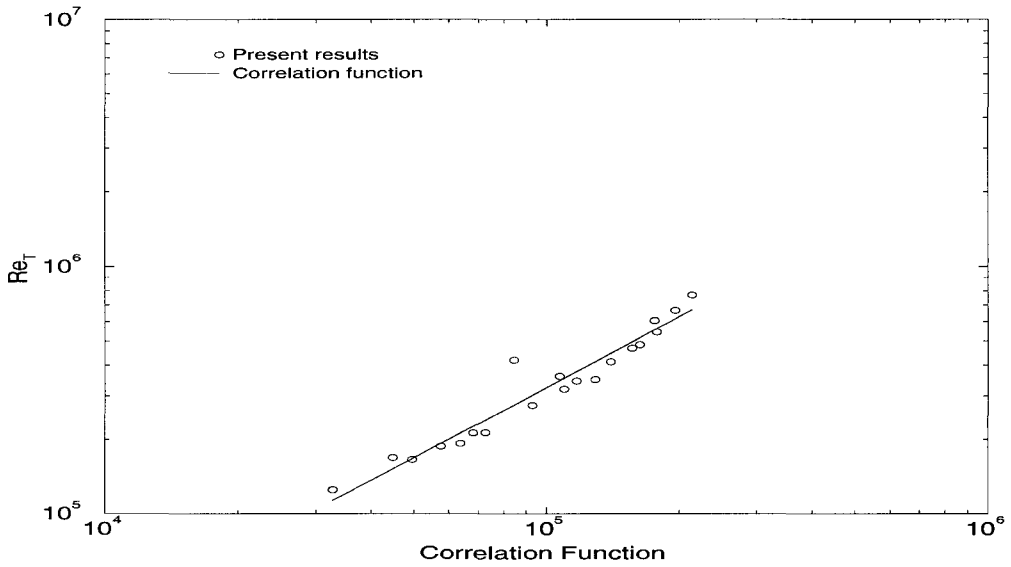

Figure 7.16 Correlation function for $Ti_\infty = 0.8\%$

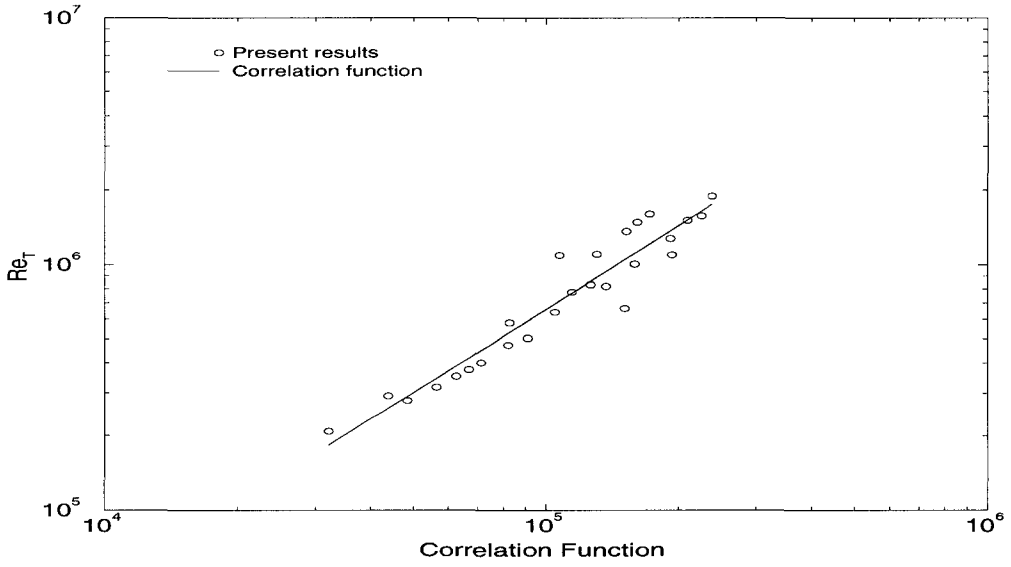

Figure 7.17 Correlation function for $Ti_\infty = 0.9\%$

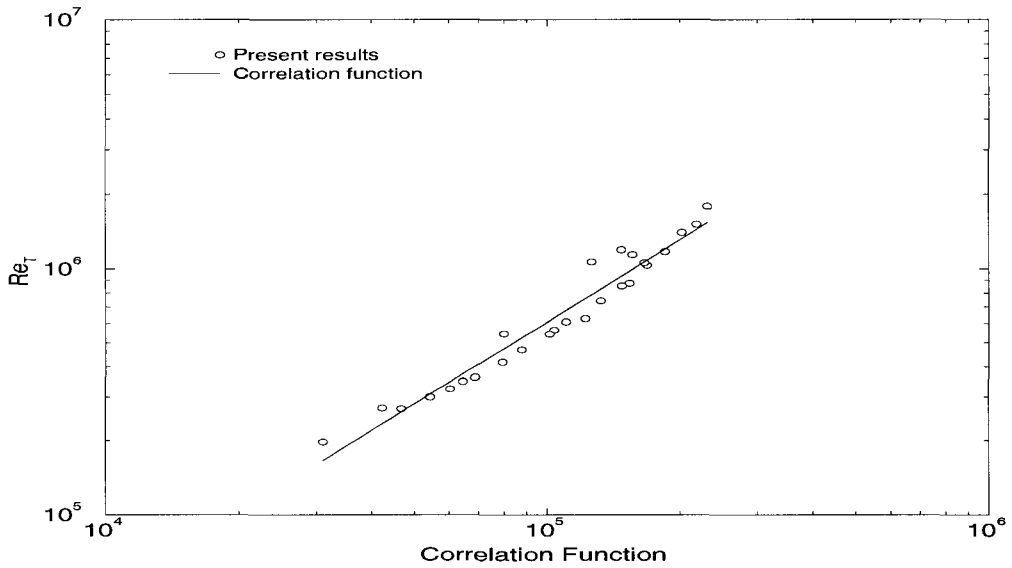

Figure 7.18 Correlation function for $Ti_\infty = 1.06\%$

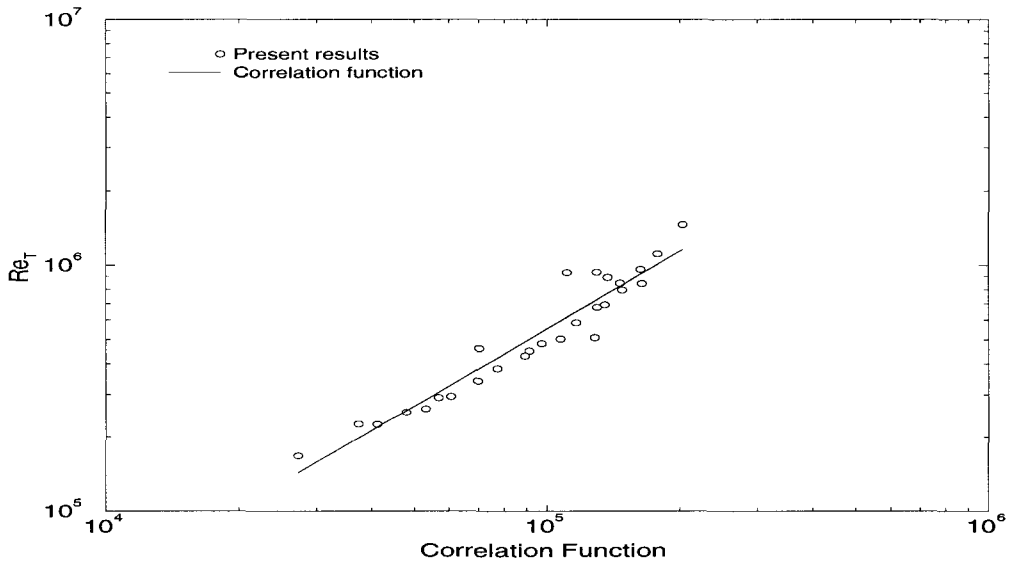

Figure 7.19 Correlation function for $Ti_\infty = 2.1\%$

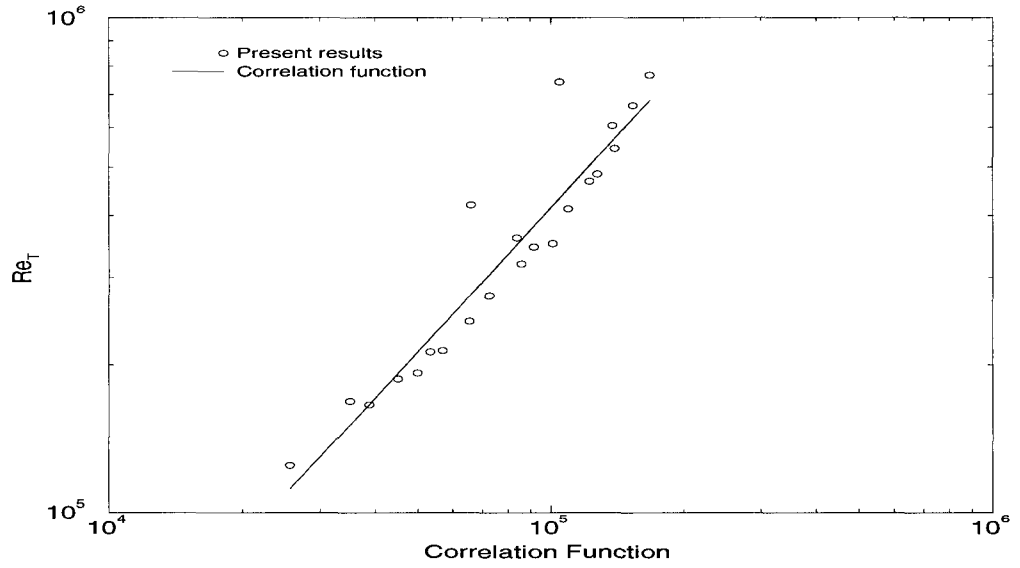

Figure 7.20 Correlation function for $Ti_\infty = 8.0\%$

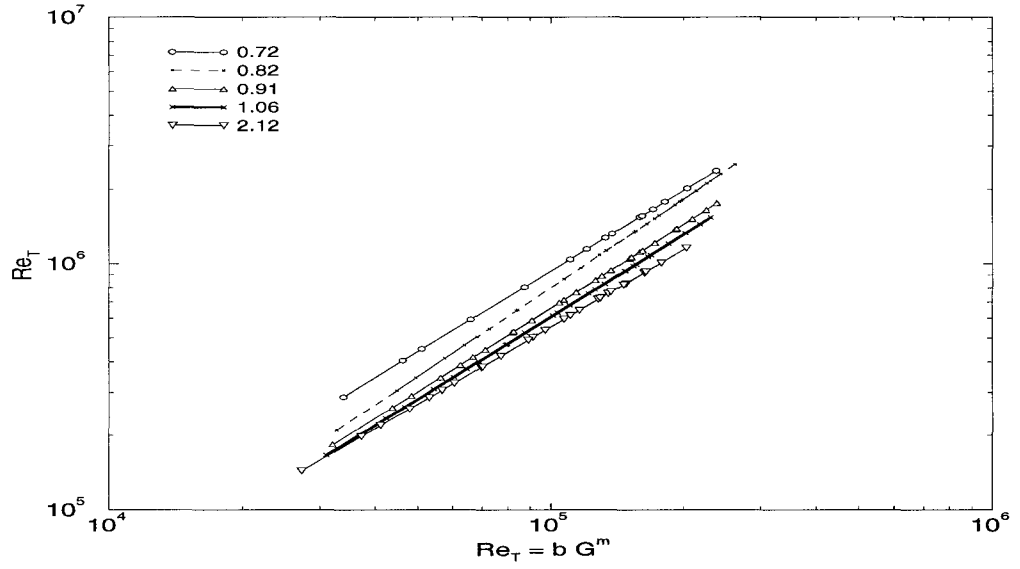

Figure 7.21 Variation of the correlation function for all values of Ti_∞

Validation of correlations

A literature survey did not yield specific values for Ti_∞ for the very limited flat plate experimental results that are available. The Ti_∞ is generally mentioned to be a *range* of values, and thus comparison with the work of other investigators is difficult at best. Nevertheless, it has been demonstrated that the trends of the M_∞ and Re_∞ variation are in excellent agreement with experiments. This has been demonstrated in Figs. 7.2, 7.7 and 7.11.

In order to validate the numerically generated data before developing the final correlation, the data was plotted using Pate's equation for planar data from Ref.[25]. The equation, as developed by Pate, is

$$Re_T = 0.0141\, {C_F}^{-2.55}\, \frac{[0.56 + 0.44\ (c_1/c)]}{(\delta^2/c)^{1/2}} \tag{7.7}$$

where C_F is the skin-friction coefficient at the onset of transition, δ is the boundary-layer thickness at the location of transition, and c_1 and c are specified constants. The results are shown in Figure 7.22. It is evident that the numerical data from the current research are in excellent agreement with Pate's correlation function for planar transition detection. This suggests that the numerical data generated in the current study correlates well with the experimental data of other investigators.

Range of validity of correlation

In using the correlations developed, it should be noted that for turbulence intensity Ti_∞ values less than 0.9 %, the error in predicting the onset of transition increases with decreasing M_∞ and decreasing Re_∞ values. The following ranges of flow parameters were used for the development of the correlation function.

$$1.97 \leq M_\infty \leq 5.0$$

$$1 \times 10^6 \leq Re/m \leq 1 \times 10^8$$

$$0.72\ \% \leq Ti_\infty \leq 2.2\ \%$$

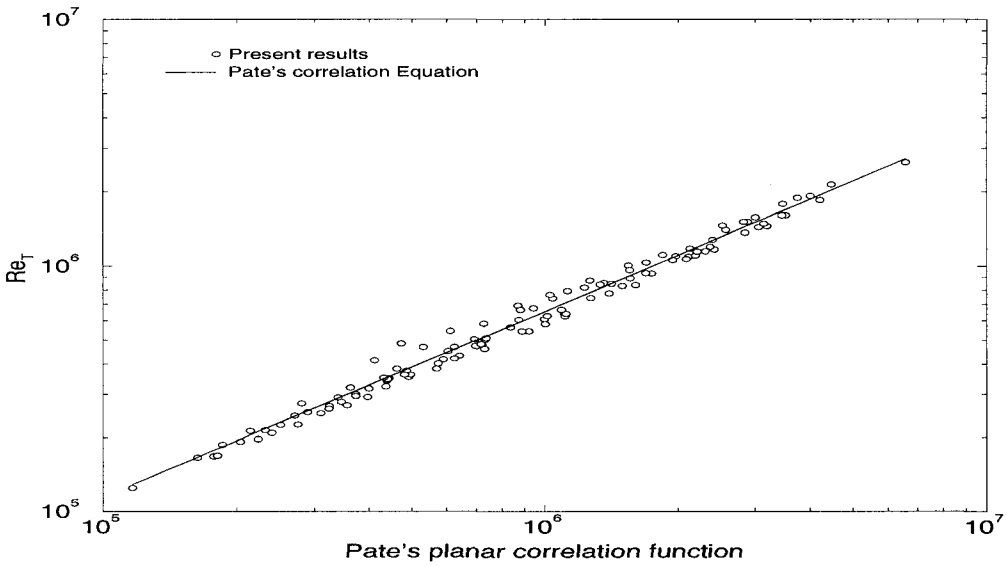

Figure 7.22 Comparison of numerically generated data with Pate' correlation function.

8 CONCLUDING REMARKS

Correlation functions have been developed to predict both the extent of the streamwise influence regions in supersonic turbulent flows and the onset of transition in supersonic flow past a flat plate. The turbulent correlation functions for a compression corner and an expansion ramp can be used along with the previously developed correlations for the shock impingement case, to predict the regions of streamwise influence for general aerodynamic bodies which usually consist of a combination of compression corners, expansion ramps and flat plate regions. The turbulent correlations for streamwise influence can be used to greatly improve the speed and efficiency of an iterative PNS numerical procedure which iterates over the region of turbulent streamwise influence to obtain accurate results. The transitional correlations can be used along with a computational code to automatically determine the onset of transition and apply a turbulence model for closure. As the correlations have been developed to depend entirely on *known* flow variables, they are very general. The functions help in understanding the physics of the phenomenon by relating the flow parameters that have a primary influence on the flow. The general form of these functions, the wide range of applicability, and their ease of calculation makes them a handy tool for engineering design purposes.

APPENDIX TABLES

Table A.1 Numerical compression ramp data

M_∞	Re/m	Re_{δ_L}	$\Delta p/p_\infty$	l_u/δ_L	l_d/δ_L
2.50	3.3200×10^7	0.01277×10^7	0.6176	0.7542	3.4591
2.50	3.3200×10^7	0.01199×10^7	1.1679	1.2217	6.5801
2.96	3.3200×10^7	0.01240×10^7	0.6210	0.5889	4.9224
2.96	3.3200×10^7	0.01311×10^7	1.3170	0.8862	6.9101
2.96	3.3200×10^7	0.01289×10^7	1.7860	1.5198	7.9854
2.96	3.3200×10^7	0.01311×10^7	2.1350	1.8738	8.0774
3.50	3.3200×10^7	0.01311×10^7	0.6210	0.5824	6.8620
3.50	3.3200×10^7	0.01311×10^7	1.9567	1.1901	7.2418
3.50	3.3200×10^7	0.01311×10^7	2.4540	1.6459	7.1658
4.00	3.3200×10^7	0.01289×10^7	1.3179	0.9016	8.0626
4.00	3.3200×10^7	0.01289×10^7	1.9572	1.1334	7.3671
4.00	3.3200×10^7	0.01265×10^7	2.6839	1.5490	7.4302
4.50	3.3200×10^7	0.01289×10^7	1.7878	1.0561	10.1491
2.50	0.3325×10^7	0.00200×10^7	0.8610	2.1264	6.7944
2.50	0.3325×10^7	0.00200×10^7	1.1680	2.4254	7.8409
2.96	1.6025×10^7	0.00720×10^7	1.0336	1.0236	6.7401
2.96	8.4910×10^7	0.02891×10^7	1.0336	0.4699	4.8724
2.96	5.0467×10^7	0.03268×10^7	1.3170	0.7351	5.5109
2.96	7.8022×10^7	0.02730×10^7	1.6210	0.7459	6.1987
2.96	8.4910×10^7	0.02971×10^7	0.4459	0.2937	4.2850
4.00	0.3325×10^7	0.00236×10^7	1.4981	2.0181	8.1852
4.50	0.3325×10^7	0.00236×10^7	0.5441	1.3830	9.2859
4.50	0.3325×10^7	0.00236×10^7	1.2917	1.9334	9.3706
4.50	0.3325×10^7	0.00236×10^7	1.7566	2.2297	9.6669
5.00	0.3325×10^7	0.00258×10^7	0.6110	1.3417	11.0823
5.00	0.3325×10^7	0.00258×10^7	1.4878	1.9610	11.2371
5.00	0.3325×10^7	0.00258×10^7	2.0305	2.2319	10.5791
5.00	0.4156×10^7	0.00294×10^7	1.2415	1.7217	11.1487
5.00	0.4156×10^7	0.00294×10^7	1.7448	2.0181	10.5560

Table A.2 Numerical expansion corner data

M_∞	Re/m	Re_{δ_L}	$-\Delta p/p_\infty$	l_u/δ_L	l_d/δ_L
2.96	3.3×10^6	2.0×10^4	0.328	1.039	4.139
2.96	3.3×10^6	2.0×10^4	0.433	1.092	5.672
2.96	3.3×10^6	2.0×10^4	0.480	1.092	6.464
2.96	3.3×10^6	2.0×10^4	0.564	1.145	7.944
2.96	3.3×10^6	2.0×10^4	0.637	1.145	9.793
2.96	3.3×10^6	2.0×10^4	0.699	1.145	12.277
2.96	3.3×10^6	2.0×10^4	0.753	1.145	14.760
2.96	3.3×10^6	2.0×10^4	0.798	1.145	15.183
2.96	3.3×10^6	2.0×10^4	0.836	1.145	16.715
2.96	3.3×10^6	2.0×10^4	0.868	1.198	18.036
2.96	3.3×10^6	2.0×10^4	0.895	1.198	19.146
2.96	6.6×10^6	3.0×10^4	0.564	0.937	7.940
2.96	6.6×10^6	3.0×10^4	0.564	0.937	9.920
2.96	2.5×10^7	9.0×10^4	0.564	0.485	7.764
2.96	2.5×10^7	1.1×10^5	0.637	0.421	7.820
2.96	2.5×10^7	9.0×10^4	0.699	0.485	11.081
2.96	2.5×10^7	9.0×10^4	0.753	0.485	14.270
2.50	3.3×10^7	1.2×10^5	0.431	0.343	3.909
2.50	3.3×10^7	1.2×10^5	0.511	0.343	4.986
3.50	3.3×10^7	1.2×10^5	0.430	0.482	7.342
3.50	3.3×10^7	1.2×10^5	0.621	0.482	12.614
3.50	3.3×10^7	1.2×10^5	0.807	0.442	20.732
4.00	3.3×10^7	1.2×10^5	0.580	0.567	14.400
4.00	3.3×10^7	1.2×10^5	0.742	0.567	22.564
4.50	3.3×10^7	1.2×10^5	0.623	0.652	20.098
4.50	3.3×10^7	1.2×10^5	0.713	0.652	24.434
4.50	3.3×10^7	1.2×10^5	0.784	0.652	27.411
2.96	3.3×10^7	1.2×10^5	0.328	0.397	4.025
2.96	3.3×10^7	1.2×10^5	0.382	0.482	4.791

Table A.3 Numerical data for onset of transition on flat plate with different criteria

M_∞	Re/m	$Re_t(min\ C_f)$	$Re_t(min\ Pressure)$
3.70	7.087×10^6	8.984×10^5	1.111×10^6
3.70	9.842×10^6	1.032×10^6	1.286×10^6
3.70	1.141×10^7	1.109×10^6	1.382×10^6
3.70	1.377×10^7	1.223×10^6	1.518×10^6
2.57	1.141×10^7	1.398×10^6	2.390×10^6
2.57	9.057×10^6	1.231×10^6	1.713×10^6
2.57	7.886×10^6	1.115×10^6	1.561×10^6
2.0	1.141×10^7	5.120×10^5	6.372×10^5
2.5	1.141×10^7	6.308×10^5	7.840×10^5
3.0	1.141×10^7	7.769×10^5	9.709×10^5
3.7	1.141×10^7	1.054×10^6	1.307×10^6
4.0	1.141×10^7	1.195×10^6	1.474×10^6

Table A.4 Constants for various Ti_∞ values

$Ti_\infty\%$	m	b
0.72	1.09	3.144
0.83	1.194	0.8509
0.91	1.127	1.5255
1.06	1.109	1.726
2.12	1.104	3.445

BIBLIOGRAPHY

[1] Zheltovodov, A.A., "Shock Waves/ Turbulent Boundary-Layer Interactions - Fundamental Studies and Applications", AIAA Paper 96-1977, June 1996.

[2] Settles, G.S. and Bogdonoff, S.M., "Scaling of Two-and Three-Dimensional Shock /Turbulent Boundary-layer Interactions at Compression Corners", *AIAA Journal* Vol 20, No. 6, 1982, pp. 782-789.

[3] Settles, G.S., Bogdonoff, S.M. and Vas, I.E., "Incipient Separation of a Supersonic Turbulent Boundary Layer at High Reynolds Numbers ", *AIAA Journal*, Vol. 14, No. 1, 1976, pp. 50-56.

[4] Delery, J. and Marvin, J.G., "Shock Wave Boundary-Layer Interactions", *AGARDograph* AG-280, Feb. 1986.

[5] Knight, D. and Yan, H., "RTO WG 10: CFD Validation for Shock Wave Turbulent Boundary Layer Interactions", AIAA Paper 2002-0437, Jan. 2002.

[6] Settles, G.S. and Dodson, L.J., "Hypersonic Shock / Boundary-Layer Interaction Database", NASA-CR 177577, Apr. 1991.

[7] Settles, G.S. and Dodson, L.J., "Hypersonic Shock/Boundary-Layer Interaction Database: New and Corrected Data", NASA-CR 177638, Apr. 1994.

[8] Hankey, W.L. and Holden, M.S., "Two-Dimensional Shock Wave-Boundary Layer Interactions in High Speed Flows", *AGARDograph* AG-203, June 1975.

[9] Law, H.C., "Supersonic Shock Wave Turbulent Boundary-Layer Interactions", *AIAA Journal*, Vol. 14, No. 6, 1976, pp. 730-734.

[10] Roshko, A. and Thomke, G.J., "Supersonic, Turbulent Boundary-Layer Interaction With a Compression Corner at Very High Reynolds Number", *Proceedings of the Symposium on Viscous Interaction Phenomena in Supersonic and Hypersonic Flow*, USAF Aerospace Research Labs, Wright-Patterson AFB, 1969, pp. 109-138.

[11] Visbal, M. and Knight, D., " The Baldwin-Lomax Turbulence Model for Two-Dimensional Shock-Wave /Boundary-Layer Interactions", *AIAA Journal*, Vol. 22, No. 7, 1984, pp. 921-928.

[12] Horstman, H.C. and Hung, C.M., "Reynolds Number Effects on Shock-Wave Turbulent Boundary-Layer Interactions - A Comparison of Numerical and Experimental Results", AIAA Paper 77-42, Jan. 1977.

[13] Chung, K., "Interaction Region of Turbulent Expansion-Corner Flow", *AIAA Journal* Vol 36, No. 6, 1998, pp. 1115-1116.

[14] Lu, F.K. and Chung, K.M., "Downstream Influence Scaling of Turbulent Flow Past Expansion Corners", *AIAA Journal* Vol 30, No. 12, 1992, pp. 2976-2977.

[15] Chew, Y.T., "Shockwave and Boundary Layer Interaction in the Presence of an Expansion Corner", *Aeronautical Quarterly* Vol XXX, Aug. 1979, pp. 506-527.

[16] Narasimha, R. and Sreenivasan, K.R., "Relaminarization of Fluid Flows", *Advances in Applied Mechanics*, Vol. 19, 1979, pp. 221-309.

[17] Ramesh, M.D., "Correlations to Predict the Streamwise Influence Regions of Two-Dimensional Turbulent Shock Separated Flows", Master's Thesis, Iowa State University, Ames, IA, Feb. 1999.

[18] Ramesh, M.D., Tannehill, J.C. and Miller, J.H., "Correlations to Predict the Streamwise Influence Regions of Two-Dimensional Turbulent Shock Separated Flows", AIAA Paper 2000-0932, Jan. 2000.

[19] Saric, W.S., " Progress in Transition Modeling", AGARD Report, AGARD-R-793, April 1994.

[20] Malik, M.R., "Boundary-Layer Transition Prediction Toolkit", AIAA Paper 97-1904, June. 1997.

[21] Coles, D., "Measurements of Turbulent Friction on a Smooth Flat Plate in Supersonic Flow", *Journal of Aerospace Sciences*, Vol. 21, No. 7, July 1954.

[22] Chen, F.J, Malik, M.R., "Boundary-Layer Transition on a Cone and Flat Plate at Mach 3.5", *AIAA Journal*, Vol. 27, No. 6, July 1989.

[23] Chen, F.J., "Boundary-Layer Transition Extent Measurements on a Cone and Flat Plate at Mach 3.5", AIAA Paper 93-0342, Jan. 1993.

[24] Pate, S.R., "Measurements and Correlations of Transition Reynolds Numbers on Sharp Slender Cones at High Speeds", *AIAA Journal*, Vol. 9, No. 6, June 1971.

[25] Pate, S.R., "Radiated Aerodynamic Noise Effects on Boundary-Layer Transition in Supersonic and Hypersonic Wind Tunnels." Reynolds Numbers on Sharp Slender Cones at High Speeds", *AIAA Journal*, March 1969.

[26] Owen, F.K., Horstman, C.C.,"Comparison of Wind Tunnel Transition and Freestream Disturbance Measurements",*AIAA Journal*, Vol. 13, No. 3, March 1975.

[27] Potter, L., " Boundary-Layer Transition on Supersonic Cones in an Aeroballistic Range", *AIAA Journal*, Vol. 13,No. 3, March 1975.

[28] Reshotko, E.,"Recent developments in Boundary-Layer Transition Research", *AIAA Journal*, Vol. 13, No. 3, March 1975.

[29] Kendall, J.M.," Wind Tunnel Experiments Relating to Supersonic and Hypersonic Boundary-Layer Transition", *AIAA Journal*, Vol. 13, No. 3, March 1975.

[30] Mack, L.M.,"Linear Stability Theory and the Problem of Supersonic Boundary-Layer Transition", *AIAA Journal*, Vol. 13, No. 3, March 1975.

[31] Low, G., " Boundary-Layer Transition at Supersonic Speeds", NACA Research Memorandum, NACA RM E56E10.

[32] Lyttle, I.J., Reed, H.L.,"Use of transition Correlations for Three-Dimensional Boundary Layers Within Hypersonic Flows", AIAA Paper 95-2293, June. 1995.

[33] Edwards, J.R., "Development of a OneEquation TransitionTurbulence Model",*AIAA Journal*, Vol. 39, No. 9, Sept. 2001.

[34] Benard, E., Sidorenko, A., "Transitional and Turbulent Heat Transfer Correlations for Swept Cylinders in Hypersonic Flow", AIAA Paper 2002-0551, Jan. 2002.

[35] Suzen, B.Y.," Predictions of Separated and Transitional Boundary layers Under Low-Pressure Turbine Airfoil Conditions Using an Intermittency Transport Equation", AIAA Paper 2001-0446, Jan. 2001.

[36] Wilcox, D.C., *Turbulence Modeling for CFD*, Second Edition, DCW Industries, La Cañada, California, 2000.

[37] Reed, H.L.,"Direct Numerical Simulation of Transition: The Spatial Approach.", AGARD Report, March 1993. Three-Dimensional Boundary Layers Within Hypersonic Flows", AIAA Paper 95-2293, June. 1995.

[38] Fasel, H.F., "DNS and LES for Investigating Transition and Transition Control", AIAA Paper 97-1820, June. 1997.

[39] Abu-Ghannam, B.J., Shaw, R., "Natural Transition of Boundary Layers - the Effects of Turbulence, Pressure Gradient and Flow History", *Journal of Mechanical Engineering Science*, Vol. 22, No. 5, 1980.

[40] Tannehill, J.C., Miller, J.H. and Lawrence, S.L., "Development of an Iterative PNS Code for Separated Flows", AIAA Paper 99-3361, June 1999.

[41] Shang, J.S. and Hankey, W.L., "Numerical Solution of The Navier Stokes equations for Supersonic Turbulent Flow Over a Compression Ramp", AIAA Paper 75-3, Jan. 1975.

[42] Shang, J.S., Hankey, W.L. "Numerical Simulation of Shock Wave -Turbulent Boundary-Layer Interaction", *AIAA Journal*, Vol 14, No. 10, 1976, pp. 1451-1457.

[43] Miller, J.H., Tannehill, J.C. and Lawrence, S.L., "PNS Algorithm for Solving Supersonic Flows with Upstream Influences", *AIAA Journal*, Vol. 38, No. 10, 2000, pp. 1837-1845.

[44] Vigneron, Y.C., Rakich, J.V., Tannehill, J.C. "Calculation of Supersonic Flow over Delta Wings with Sharp Subsonic Leading Edge", AIAA Paper 78-1209, July 1978.

[45] Lawrence, S.L., Chausee, D.S. "Upwind Algorithm for the Parabolized Navier-Stokes Equations", *AIAA Journal* Vol. 27, No. 9, Sept 1989, pp. 1175.

[46] Miller, J.H., Tannehill, J.C. "Computation of Supersonic Flows with Embedded Separated Regions Using an Efficient PNS Algorithm", AIAA Paper 97-1942, Jan. 1997.

[47] Tannehill, J.C., Anderson, D.A., and Pletcher, R.H. *Computational Fluid Mechanics and Heat Transfer.* 2nd edition, Taylor and Francis, Washington D.C., 1997.

[48] Baldwin, B.S., MacCormack, K.W. "Modifications of the Law of the Wall and Algebraic Turbulence Modeling for Separated Boundary Layers", AIAA Paper 76-350, July 1976.

[49] Cebeci, T., Smith, A.M.O., Mosinskis, G. "Calculation of compressible adiabatic turbulent boundary layers", *AIAA Journal* Vol. 8, No. 11, June 1969, pp. 1974.

[50] Bradshaw, P. "Effects of Streamline Curvature on Turbulent Flow", *Agardograph* AGARD-AG-169, Aug. 1973.

[51] Viegas, J.R. and Horstman, C.C., "Comparison of Multi-equation Turbulence Models for Several Shock Separated Boundary-Layer Interaction Flows", AIAA Paper 78-1165, July 1978.

[52] Jones, W.P., "Calculation of Low Reynolds Number Phenomena with a two-equation Model of Turbulence." , *International Journal of Heat and Mass Transfer*, Vol. 16, 1973.

[53] Wilcox, D.C., "Simulation of Transition with a Two-Equation Turbulence Model", *AIAA Journal*, Vol. 32, No. 2, Feb. 1994.

[54] Wilcox, D.C., "Turbulence-Model Transition Predictions.", *AIAA Journal*, Vol. 13, No. 2, January 1975.

[55] Buning, P.G. Jespersen, D.C., Pulliam, T.H., *OVERFLOW Manual*, Version 1.7v, NASA Ames Research Center, Moffett Field, California, June 1997.

[56] Urbin, G. and Knight, D.,"Compressible large Eddy Simulation using Unstructured Grid: Supersonic Turbulent Boundary layer and Compression Corner", AIAA Paper 1999-0427, Jan. 1999.

[57] Reda, D.C. and Murphy, J.D. "Shock Wave/Turbulent Boundary-Layer Interactions in Rectangular Channels", *AIAA Journal*, Vol. 11, No. 2, 1973, pp. 139-140.

[58] Reda, D.C. and Murphy, J.D. "Sidewall Boundary-Layer Influence on Shock Wave/Turbulent Boundary-Layer Interactions", *AIAA Journal*, Vol. 11, No. 10, 1973, pp. 1367-1368.

[59] Ramesh, M.D. and Tannehill J.C., "Correlations to Predict the Streamwise Influence Regions in Supersonic Turbulent Flows ", *Journal of Aircraft*, to be published, Nov/Dec 2003.